Probing the Hydrogen Bonding Interaction at the Gas-Surface Interface using Dispersion Corrected Density Functional Theory

Angela Celeste Edwards

Thesis submitted to the faculty of the Virginia Polytechnic Institute and State University in partial fulfillment of the requirements for the degree of

Master of Science
In
Chemistry

Diego Troya, Chair
John R. Morris
T. Daniel Crawford

December 3rd, 2014
Blacksburg, Virginia

Keywords: silica, chemical warfare agents, computational chemistry, adsorption, binding energy

Probing the Hydrogen Bonding Interaction at the Gas-Surface Interface using Dispersion Corrected Density Functional Theory

Angela Celeste Edwards

ABSTRACT

The interactions of the chemical warfare agent sulfur mustard with amorphous silica were investigated using electronic structure calculations. In this thesis, the binding energies of sulfur mustard and mimic species used in the laboratory were calculated using density functional theory and fully ab initio calculations. The wB97XD and B97D functionals, which include functions to account for long-range dispersion interactions, were compared to experimental trends. The hydroxylated amorphous silica surface was approximated using a gas-phase silanol molecule and clusters containing a single hydroxyl moiety.

Recent temperature programmed desorption experiments performed in UHV concluded that sulfur mustard and its less toxic mimics undergo molecular adsorption to amorphous silica. Hydrogen bonding can occur between surface silanol groups and either the sulfur or chlorine atom of the adsorbates, and the calculations indicate that the binding energies for the two hydrogen bond acceptors are similar. The adsorption of sulfur mustard and its mimics on silica also exhibits the presence of significant van der Waals interactions between alkyl of the adsorbates and the surface. These interactions, in combination with the formation of a hydrogen bond between a surface silanol group and the Cl or S atoms of the adsorbates, provide remarkably large binding energies.

Acknowledgements

I would like to begin by thanking my family. My mother, father, sisters, and Uncle Cy have supported all I do since birth. I would like to thank my friends Melanie, Melissa, and Michelle for providing long distance support and encouragement. I am thankful for Rachele and her family for adopting me as one of theirs during my time at Virginia Tech. Also, I am grateful for Alex, who has been exactly the support I needed while completing my thesis.

I would also like to thank my advisor Dr. Diego Troya for his guidance and wisdom in all of my research. He has taught me to be more thoughtful in my work and words, increasing my scientific vocabulary and understanding. I thank him for sharing his knowledge and time with me and truly appreciate his effort and patience. I am also grateful to my advisory committee, Dr. Daniel Crawford and Dr. John Morris, who has treated me like one of his students.

Finally, I would like to thank and acknowledge my colleagues. I would like to express my gratitude to the other member of my group, Robert Chapleski, and the members of my extended group, Joshua Abelard, Steve Burrows, Chikki Chan, Darren Driscoll, Dallas Mann, Cecilia Smith, Guanyu Wang, and Yafen Zhang, who all helped me navigate graduate school. Lastly, I would like to thank the people of the Theory Lab, specifically Harley, for proof reading my thesis and providing quick lessons in linear algebra.

Table of Contents

Table of Figures

Table of Abbreviations

IR	Infrared Spectroscopy
TPD	Temperature Programmed Desorption
CWA	Chemical Warfare Agent
IUPAC	International Union of Pure and Applied Chemistry
HA	Hydrogen Bond Acceptor
UHV	Ultra-High Vacuum
IR	Infrared Spectroscopy
XPS	X-Ray Photoelectron Spectroscopy
MDCP	Methyl dichlorophosphate
VX	O-ethyl S-[2-(diisopropylamino)ethyl] methylphosphonothioate
DMMP	Dimethyl methylphosphonate
MP2	Möller-Plesset 2nd Order Perturbation Theory
DMCP	Dimethyl chlorophosphate
TMP	Trimethyl phosphate
DIMP	Diisopropyl methylphosphonate
HD	Sulfur mustard
DES	Diethyl sulfide
2-CEES	2-chloroethyl ethyl sulfide
HF	Hartree-Fock
DFT	Density Functional Theory
LDA	Local Density Approximation
GGA	General Gradient Approximation
LSDA	Local Spin Density Approximation
B3LYP	Becke-3 parameter-Lee, Yang, Parr
LYP	Lee, Yang, Parr
B97D	Becke 97-D
STO	Slater-type Orbital
GTO	Gaussian-type Orbital
LCAOs	Linear Combination of Atomic Orbitals
BSSE	Basis Set Superposition Error
MO	Molecular Orbital
HOMO	Highest Occupied Molecular Orbital
LUMO	Lowest Unoccupied Molecular Orbital

Chapter 1 – Motivation, Background, and Experimental Work

1.1. Research Motivation and Background

The unique chemical environment present at a surface accommodates for interaction phenomena with gases that are not possible in the bulk of the material.[1] In order to capture the nature of these distinctive gas/surface phenomena, characterization techniques such as infrared spectroscopy (IR) or temperature programmed desorption (TPD) are used to give insight into the interaction mechanism and its strength.[2] One type of mechanism is physisorption, which is illustrated as hydrogen bonding in Figure 1. In physisorption, the exposed atoms at the solid interface can interact with a gas-phase molecule without the breaking or formation of covalent bonds.[3] The type and strength these interactions give insight into the adsorption mechanism at the gas-surface interface.

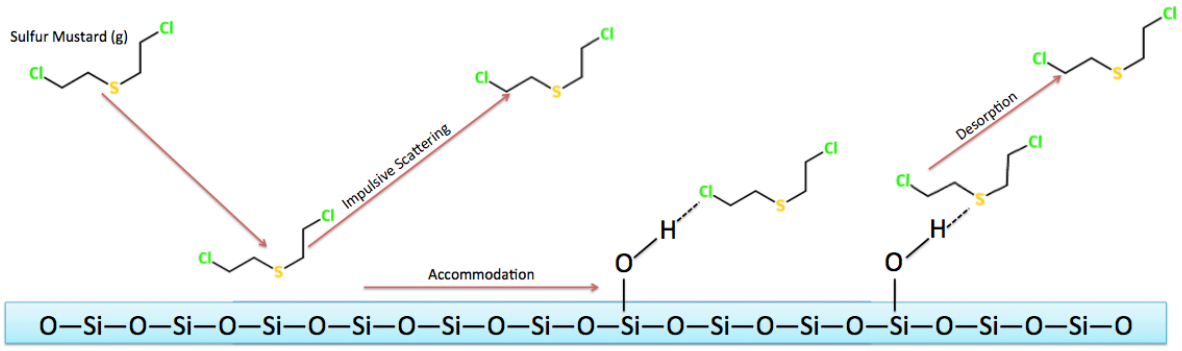

Figure 1. The interaction of sulfur mustard with a silica surface.[4]

One specific gas-surface interaction of interest is that of chemical warfare agents and amorphous silica. Dispersed toxic agents such as sulfur mustard (bis (2-chloroethyl) sulfide, a vesicant) and sarin ((RS)-propan-2-yl methylphosphonofluoridate, a nerve agent) gases, result in harmful and potentially deadly biological reactions. The interaction of these chemical warfare agent (CWA) gas molecules with biological surfaces is where the bodily reaction begins. The bodily reactions can result in blisters, seizures, asphyxiation, and death.[5] Due to their inherent

toxicity and their use during international conflict, method development for decontamination of chemical warfare agents has been paramount.[6]

In order to study the CWAs and their interactions, chemical simulants are selected to mimic the structural and functional components of the active chemical warfare agent while reducing hazards.[7] For example, a mimic for mustard gas (HD), seen in Figure 1, is diethyl sulfide (DES). DES, while structurally similar to HD, lacks the terminal chlorine atoms of the active agent. DES is used to isolate just the sulfur atom moiety in HD. All mimics in this work were selected so as to isolate a moiety of the active agent. The interaction of a moiety with surface can be probed independent of other interactions by isolating that single moiety. The goal of this research is to investigate the binding of CWAs on surfaces at a fundamental level using a variety of techniques.

This thesis focuses on surface interactions and gives insight into the adsorption of CWAs and their mimics on silica. Hydrogen bonding and its role in CWA adsorption is discussed in detail. The research results are used to describe the unique binding characteristics of various CWA and mimic adsorbates. A detailed discussion of molecular orbital theory and bond acidity is used to elucidate the nature of binding interactions. Finally, the future of this work is discussed.

1.2. Gas-Surface Interaction

1.2.1. Adsorption

The adsorption of a molecule onto a surface can occur through chemisorption or physisorption. Chemisorption is a chemical interaction between a surface and an adsorbate, that can result in the decomposition of gases such as CWAs.[8-12] In contrast, physisorption arises from physical interactions, such as hydrogen bonding, which may lead to the non-destructive

desorption of the adsorbate. Whether an adsorbate undergoes chemisorption or physisorption is determined by the properties of the adsorbate and surface.[13]

The adsorption of gas molecules on a surface can result in monolayers or multilayers through either chemical or physical interactions.[14] Monolayers are the result of a single adsorbate interacting with one or more domains on the surface. However, an adsorbate can form multilayers by interacting with another adsorbate through physical processes, such as hydrogen bonding. These interactions result in the growth of the adsorbate layers, which have different kinetic and energetic consequences than those of a monolayer. Various models have been proposed to describe the formation of these layers.[1] The assumptions, advantages, and disadvantages of the Langmuir model used to describe temperature programmed desorption are discussed below.

1.2.1.1. Models of Adsorption

Langmuir Monolayer Model

Irving Langmuir, in 1918, derived a theory to model the kinetics of adsorption of a monolayer of gas on a surface.[14,15] His model assumes that (i) the surface is homogenous, (ii) there are specific interaction sites on the surface, (iii) a site on the surface can only interact with one adsorbate, and (iv) there is no change in phase.[16] These assumptions were conclusions drawn from Langmuir's original work,[17] where he measured the changes in properties of metals, such as catalytic ability, before and after exposure to a known amount of gas. Although this model has several inaccuracies, such as the neglect of multiple adsorbates binding to one surface site and the formation of multilayers,[7] it is still utilized today to calculate surface coverage as a function of reaction kinetics.

One must consider the rate of adsorption at the gas-surface interaction to calculate the surface coverage by an adsorbate.[14] The ratio of the rates of adsorption and desorption must reach unity at equilibrium and can be described by the equations

$$Rate_{adsorption} = k_a\, p_A[S] \tag{1}$$

and

$$Rate_{desorption} = k_d\, [A_{ad}] \tag{2}$$

where k_a and $k_d$are the rate constants for adsorption and desorption, respectively, p_A is the partial pressure over the surface, $[S]$ is the concentration of unbound sites, and $[A_{ad}]$ is the concentration of bound adsorbate. At equilibrium:

$$\frac{[A_{ad}]}{p_A[S]} = \frac{k_a}{k_d} = K_{eq}^A. \tag{3}$$

K_{eq}^A, or the equilibrium constant, is commonly referred to as the Langmuir adsorption constant α, and is unique to a particular system. Assuming that the initial surface binding sites, or S_0, is equal to

$$[S_0] = [S] + [A_{ad}] \tag{4}$$

Equation (3) becomes

$$[S_0] = \frac{1+K_{eq}^A\, p_A}{K_{eq}^A\, p_A}[A_{ad}]. \tag{5}$$

The fraction of adsorbate bound to the surface at equilibrium over the total number of sites gives rise to $\boldsymbol{\theta_A}$, or surface coverage, which can be expressed as

$$\theta_A = \frac{[A_{ad}]}{[S_0]} = \frac{K_{eq}^A\, p_A}{1 + K_{eq}^A\, p_A} = \frac{\alpha\, p_A}{1 + \alpha\, p_A}. \tag{6}$$

This derivation shows that the coverage of a surface by a monolayer of gas molecules can be calculated by knowing the pressure and the equilibrium constant of adsorption, which is the ratio of adsorption and desorption rate constants. These rate constants are dependent upon the binding energy, which is the primary focus of this work.

Other Models

Brunauer, Emmett, and Teller, in a continuation of Langmuir's work, proposed an extension to the monolayer model which would include the effect of weak intermolecular interactions that result in the formation of multilayers.[18,19] Their kinetic model assumed that the same forces present as a gas condenses, such as hydrogen bonding and van der Waals forces, could result in the formation of multilayers.[19,20] In a further attempt to accurately describe the adsorption kinetics, Kisliuk proposed a model which described the inhomogeneity of gas adsorption as a function of sticking probability and local surface environment.[21,22] These models, while describing the kinetics of adsorption, do not describe the interaction between adsorbate and surface. To understand these interactions, it is important to know the nature of the intermolecular interaction.

1.2.2. Intermolecular Interactions

Intermolecular interactions, such as hydrogen bonding, occur as gas molecules approach a surface. In the gas-surface case, the strength and type of intermolecular interaction is dependent on the chemical nature of the adsorbate and surface. The chemical nature of the surface and adsorbate can be studied experimentally.[3]

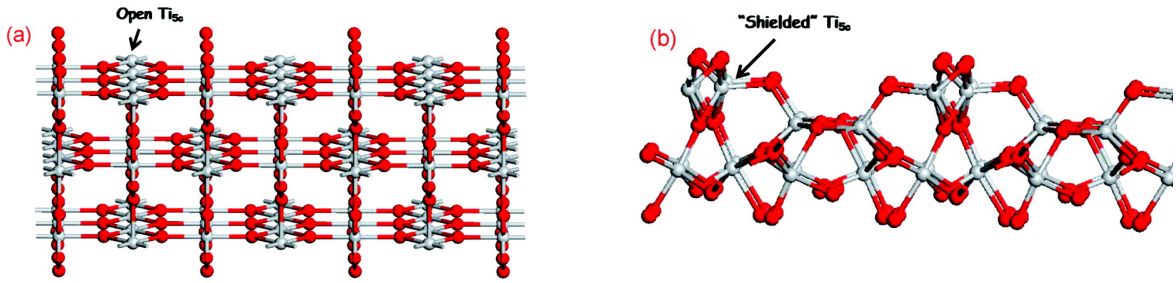

Figure 2. Models of TiO_2 where Ti atoms are grey and O atoms are red. The chemical environments for rutile 110 (a) and rutile 011 (b) TiO_2 differ. Reprinted with permission from Tao, et al.[23] Copyright 2011. American Chemical Society.

While the bulk of the solid material does not play a significant role in the adsorption of gas molecules, the outermost layer provides binding sites with chemical environments that allow for adsorption.[3,24] An example of how the surface characteristics influence adsorption is how rutile 110 and rutile 011 TiO_2 surfaces adsorb gaseous acetic acid differently under identical conditions.[23] The index attached to rutile TiO_2, or Miller notation, indicates the plane of the crystal lattice structure.[25] The different electronic and spatial structures of the TiO_2 crystals are shown in Figure 2. Both rutile 110 and 011 have five-coordinate titanium (Ti_{5c}) atoms. However, in rutile 110, these Ti_{5c} atoms are separated by three-coordinate oxygen atoms (O_{3c}) which create 'openings' that allow gas molecules to adsorb. The Ti_{5c} atoms of rutile 011 are surrounded by two-coordinated oxygen (O_{2c}) atoms in a bent geometry, which obscures the titanium atoms and decreases adsorption.[26] The decrease in adsorption due to steric hindrance in rutile 011 is evidence of the surface characteristics' impact on adsorption.

1.2.2.1. Hydrogen Bonding Interaction and Surface Hydroxyl Density

Experiments determined that certain CWAs interact with amorphous silica by hydrogen bonding to hydroxyl groups at the surface.[4,7,27-29] The infrared data indicates that the hydrogen bonds between the surface and CWA cause red shifts of the surface's hydroxyl stretching mode and result in large binding energies when compared to the hydrogen bond dimer in water. The fundamental nature of hydrogen bond and the hydrogen bond interaction between the adsorbates

and the surface was probed in this research.

The hydrogen bond was originally described the attraction between hydrogen and nitrogen, oxygen, or fluorine atom. However, The International Union for Pure and Applied Chemistry (IUPAC) currently defines the hydrogen bond as an interaction between a X-H moiety, where X is more electronegative than H, and another atom that is intramolecular or intermolecular where there is evidence of bond formation.[30] Hydrogen bonds are the result of a combination of forces, including electrostatic forces, charge transfer, covalent binding, and dispersion forces between an X-H moiety and another atom.[31-42]

The hydrogen bonding interaction requires the consideration of more than one parameter, such as orbital overlap.[30] First, convention makes the X-H moiety the hydrogen bond donor (H_B-D). The hydrogen bond donor is drawn to the electron density on the hydrogen bond acceptor (A). The hydrogen bond acceptor is usually an electron rich environment, such as an atom with lone pair electrons. Simultaneously, the hydrogen bond acceptor donates electron density to the σ^* orbital on X-H and forms the hydrogen bond which in turn weakens the X-H bond. Research has shown that the smaller the energy difference between the lone pair electron orbital on the acceptor is to the energy of the σ^* orbital on X-H, the stronger the hydrogen bond.[34,35,39,42] In addition, the acidity of the H_B-D hydrogen atom influences the strength of the hydrogen bond. Gu et al.[35] determined that the adsorption energy of the adsorbate-silica dimer will change linearly with the acidity of the donor, which was determined using natural bond order analysis and infrared spectroscopy. Another parameter that affects the hydrogen bonding strength is the proton affinity of the acceptor.[31-33,36,39] Recent work has shown a correlation between the proton affinity and dissociation energy of the hydrogen-bonded complex.[31,36,39] Biswal, et al.[32,33] concluded that the proton affinity of the acceptor, also computed through

natural bond order analysis, influenced the hydrogen bonding energy but did not correlate directly to frequency shifting of the donor hydroxyl stretch upon binding. The hydrogen bonding strength can also be related to the structure of the adsorbate and surface.

The energy of adsorption is dependent on the characteristics of the adsorbate[7,43] as well as those of the surface. In the case of amorphous silica, the density and type of hydroxyl groups on the surface affects the adsorption energy. On a silica surface, there are three types of hydroxyl groups; free or isolated, geminal, and vicinal.[24,44] These groups, seen in Figure 3a, are in spatially and chemically different environments. Isolated silanol groups are located more than one —O—Si—O— moiety from each other. In contrast, geminal silanol groups are located on the same silicon atom and vicinal silanol groups are located on neighboring silicon atoms.

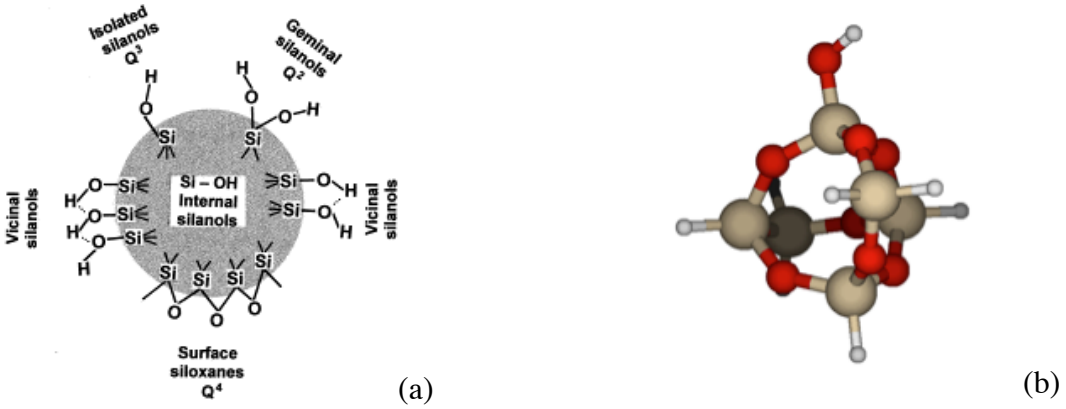

Figure 3. (a) Types of hydroxyl groups on silica[45] and (b) the structure of a silica cluster.7 Tan is silicon, white is hydrogen and red is oxygen. Reprinted from Colloids and Surfaces A,[173], Zhuravlev, The surface chemistry of amorphous silica, Copyright 2000, with permission from Elsevier.

The density and type of hydroxyl groups on a silica surface depend on the external conditions to which the surface is exposed.[24] For example, experimentalists utilize silica that has been annealed to high temperatures under ultra-high vacuum (UHV) conditions, which remove ambient gases.[45] The exposure to high temperatures and a clean environment results in a surface that is primarily isolated hydroxyl groups, a model of which is seen in Figure 3b. In Table 1, the

silanol concentration dependence on treatment temperature is shown. These silanol concentrations can be determined by deuterium-exchange and infrared spectroscopy.[45]

Table 1. The hydroxyl group density and their average distance on silica at various temperatures. Adapted with permission from Zhuravlev.[45] Reprinted from Colloids and Surfaces A,[173], Zhuravlev, The surface chemistry of amorphous silica, Copyright 2000, with permission from Elsevier.

Temperature of vacuum pretreatment (°C)	Total OH groups (OH/nm^2)	Free OH groups (OH/nm^2)	Geminal OH groups (OH/nm^2)	Vicinal OH groups (OH/nm^2)	Average distance between two free OH groups (nm)
180-200	4.60	1.20	0.60	2.80	0.76
300	3.55	1.65	0.50	1.40	0.73
400	2.35	2.05	0.30	0	0.74
500	1.80	1.55	0.25	0	0.84
600	1.50	1.30	0.20	0	0.92
700	1.15	0.90	0.25	0	1.05
800	0.70	0.60	0.10	0	1.35
900	0.40	0.40	0	0	1.79
1000	0.25	0.25	0	0	2.26
1100	0.15	0.15	0	0	2.91
1200	0	0	0	0	--

The strength of hydrogen bonding between organophosphorous agents and silica was recently studied as a function of hydroxyl density. In a recent paper by Taylor et al.,[44] the authors compared previous theoretical binding energies to those determined by inverse gas chromatography. They proposed that the strength of the binding energy is a result of the type of silanol group, which suggests that strongest hydrogen bonds occur between CWAs and vicinal hydroxyls. They also determined that there was good agreement between theory and experiment for some organophosphorous CWAs and their mimics, but not all, and suggested additional research to probe hydrogen bonding interactions to determine the cause of the discrepancies. Quenneville et al.[46] determined that changing the silanol density affects the amount of hydrogen bonding between organophosphorous CWAs and silica. They determined that high hydroxyl density resulted in primarily hydrogen bonding interactions. At lower hydroxyl densities, some mimics of Sarin covalently bind to the surface and undergo decomposition.[46] The research

suggests that vicinal hydroxyl groups at a high density result in the strongest physisorption of organophosphorous CWAs to silica.

Hydroxyl density has been shown to affect the hydrogen bonding interaction of CWAs with silica. Additional characterization of these interactions can be done using various experimental techniques, such as monitoring changes in the surface and adsorbate.

1.2.2.2. Experimental Methods of Characterizing Gas-Surface Interactions

Surface features and gas adsorption can be characterized experimentally with a variety of techniques. These techniques include infrared spectroscopy (IR), x-ray photoelectron spectroscopy (XPS), and temperature programmed desorption (TPD). Each of these techniques results in specific information that furthers insight into the system.

Infrared Spectroscopy

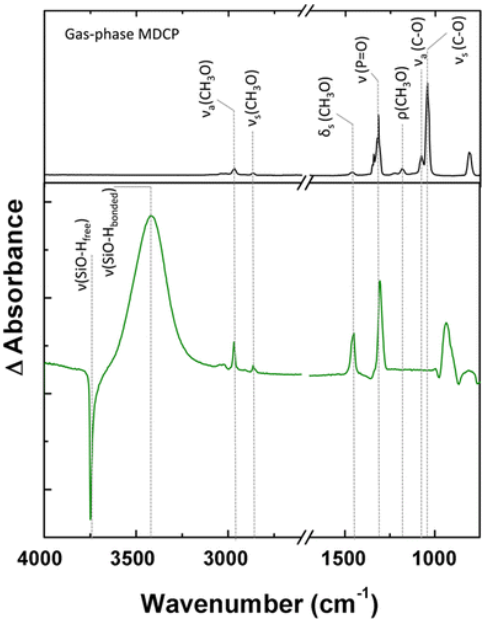

Figure 4. Gas-phase IR spectra of MDCP (top) and MDCP adsorbed on silica (bottom). Reprinted with permission from Wilmsmeyer, et al.[7] Copyright 2013, American Chemical Society.

IR uses a compound's structurally dependent ability to absorb infrared radiation to probe the vibrational modes. IR is used to determine the evolution of the adsorbate-surface interaction. This is done by monitoring the intensity of a vibrational mode of the surface or adsorbate as a

function of time. A surface vibrational mode that does not change upon exposure to the adsorbate is not involved in the adsorbate-surface interaction. However, a change in the mode's intensity denotes a change in the environment[47] which occurs when a gas molecule hydrogen bonds to a hydroxyl group in silica. The 'free' hydroxyl vibrational mode intensity decreases as hydrogen bonds form. This hydroxyl stretching mode shifts are shown in Figure 4 in the 3400-3800 cm^{-1} region.

This technique was recently used to study the interaction of methyl dichloromethylphosphate (MDCP), a mimic of the CWA Sarin, with a silica surface.[7] In Figure 4, the peaks in the IR spectra of MDCP and MDCP on silica are labeled with the corresponding vibrational modes. The difference spectrum, bottom, indicates how the intensity of the vibrational modes change after exposure to adsorbate when compared to the background spectra of clean silica. The vibrational mode of free hydroxyls on clean silica is located at 3748 cm^{-1}. The decrease in the free OH mode intensity in the difference spectrum is the result of the formation of hydrogen bonds between the surface hydroxyl groups and MDCP. The formation of these hydrogen bonds causes the intensity to increase in the bonded hydroxyl stretch around 3400 cm^{-1}. The red shift of the hydroxyl-stretching mode upon hydrogen binding is discussed in detail in Section 3.2.2. The spectra in Figure 4 are evidence of MDCP hydrogen bonding to a silica surface.

X-Ray Photoelectron Spectroscopy

XPS is a surface-sensitive method that can identify the atoms present at the surface. In this technique, a surface is irradiated with x-rays and the energy of the resultant photoelectrons released from the surface is determined.[48] The kinetic energy and peak ratios of these electrons are correlated to the element and atomic orbital from which they escaped. XPS can be performed

prior to and after the exposure of a surface to an adsorbate but is challenging to operate in real time during gas exposure.[49,50]

A recent application of XPS investigated the interaction of CWA mimics of mustard gas to an aminoferrocene surface for the purpose of CWA detection.[51] Due to a shift in the nitrogen 1s photoelectron energy of surface amino groups, it was determined that the CWAs interacted with the amino group. This was supported by the lack of shift in all other atoms in the aminoferrocene surface. It was confirmed that the mimics undergo hydrogen bonding to the surface amino groups by IR spectroscopy.

Temperature Programmed Desorption

TPD is used to probe activation energy of desorption and desorption products for reactions of molecules on surfaces. The surface, in UHV conditions to ensure cleanliness, is exposed to the gaseous adsorbate. Then, the adsorbate will desorb as the temperature is raised when it achieves the activation energy of desorption.[4] The desorbed gas species is detected by a mass spectrometer and the resultant spectrum of desorption intensity versus temperature can be fit to a Redhead model to determine the binding energy.[52] When raising the temperature the equation for temperature becomes

$$T = T_0 + \beta t \tag{7}$$

where T is the temperature, T_0 is the initial temperature, t is the time and β is a constant. The rate of desorption, r_d, would depend on the fraction of the surface covered by the adsorbate, θ_A, which is expressed as

$$r_d = -\frac{d\theta}{dt} = k\theta_A \ . \tag{8}$$

The rate changes as a function of first order rate constant, k, and on the surface coverage. The rate constant is expressed as

$$k = Ae^{\frac{-E_d(\theta_A)}{RT}} \tag{9}$$

where A is a pre-exponential factor unique to the system, E_d is the activation energy of desorption, and R is the gas constant. Replacing A with the common ν_n, the rearrangement of equations 7-9 gives rise to the Polyani-Wigner equation,[4]

$$r = -\frac{d\theta}{dt} = \nu_n(\theta_A)\,\theta_A e^{\left(-\frac{E_d(\theta_A)}{RT}\right)} \quad . \tag{10}$$

The pre-exponential factor and activation energy can be solved by fitting the desorption spectra (intensity versus temperature) of various surface coverages.

Recent applications of TPD include the investigation of the interaction of CWA mimics on silica surfaces. The TPD results indicated that the activation energy of desorption for Sarin gas mimics are in the 40-60 kJ/mol range.[7,29] Additionally, the mass spectrum of the desorption product confirmed the molecular integrity of the product, indicative of a non-destructive physisorption interaction. These TPD studies, in conjunction with IR data, concluded that physisorption by means of hydrogen bonding to surface hydroxyl groups was the primary intermolecular interaction for CWA and silica systems.

IR, XPS, and TPD can be used to study the interactions of CWAs with common surfaces such as amorphous silica and metal oxides. [53-57] The Morris Group at Virginia Tech is currently employing these techniques to study the interaction of sulfur mustard gas to silica surfaces in UHV conditions.

1.3. Chemical Warfare Agents

Contemporary chemical warfare agents emerged during World War I.[58] Sulfur mustard, a vesicant, was primarily dispersed as a gas, which would cause painful burns to exposed flesh. An estimated 70% of CWA fatalities in War World I are attributed to HD exposure.[59] Despite an

international United Nations treaty signed in 1997,[5] the threat of CWAs use has continued into modern times.

1.3.1. Chemical Warfare Agents and Surfaces

Decontamination and disposal procedures are outlined by the United States military to combat personal injury and exposure.[6] For non-disposable materials, however, the interactions of CWAs require additional attention. Adsorption of CWAs to surfaces, such as glass, sand, and metal oxides, has garnered great interest in recent years.[4,7-10,12,13,29,43,46,51,60-78]

1.3.2. Intermolecular Interactions of Chemical Warfare Agents

On amorphous silica, CWAs adsorb primarily by hydrogen bonding to surface hydroxyl groups.[4,7,13,29,44,46,67,72,75,79] On other surfaces such as metal oxide surfaces, which include TiO_2,[76,61,61] $\propto$-Fe_2O_3,[66] and Al_2O_3,[43,60,61] organophosphorous CWAs can adsorb and decompose. These decomposition reactions are dependent on the surface structure, degree of hydroxylation, and reaction temperature. At low temperatures, the molecular adsorption of organophosphorous agents is a result of hydrogen bonding between the phosphoryl oxygen atom and the silanol groups on silica or acidic portions on TiO_2. At high temperatures, the phosphoryl oxygen undergoes chemisorption to TiO_2 and decomposition occurs.[9] Similar adsorption characteristics were seen on other metal oxides, such as silver[74,80] and yttrium[8] oxide nanoparticles. While physisorption was evident on a variety of metal oxide surfaces, the type and strength of these interactions is surface and adsorbate specific.

1.3.2.1. Binding Domains on Chemical Warfare Agents and Mimics

The chemical and physical structure of CWAs impacts the strength of binding to the surface. For example, the conformation of a CWA has been determined to affect the binding energy. In the investigation of organophosphorous CWAs, multiple conformations were

explored for each species using electronic structure calculations.[11,72,75] The lowest-energy structure was then used to identify the electron-rich groups of the mimic that could act as hydrogen-bond acceptors.[75]

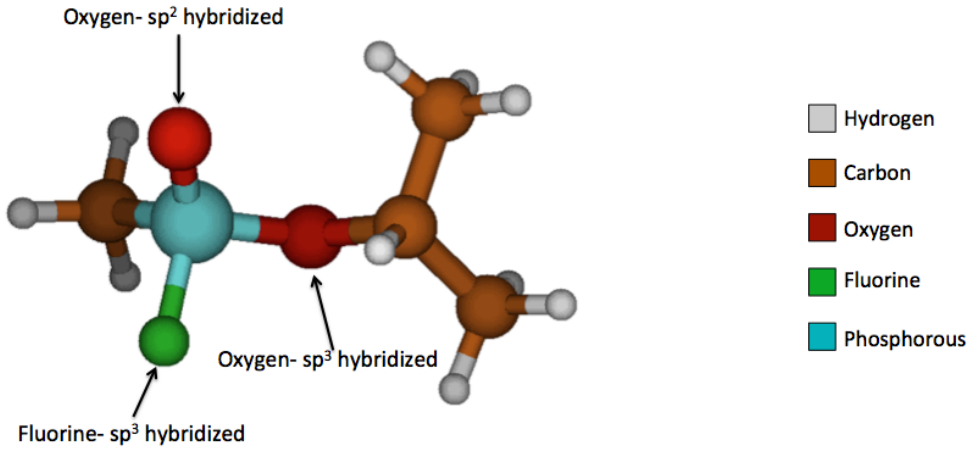

Figure 5. Hydrogen bond accepting atoms of Sarin, including the sp^2 hybridized oxygen atom of the phosphoryl group, the sp^3 hybridized oxygen atom of the alkyoxy group, and the sp^3 hybridized Fluorine atom.

In the Sarin molecule, there are three hydrogen bond donating groups, identified in Figure 5, including the sp^2-hybridized oxygen, the sp^3-hybridized oxygen and the halogen atom. *Ab initio* calculations indicated that the binding energies to a silica cluster of these three hydrogen-bond acceptors followed the trend: sp^2 oxygen > sp^3 oxygen > fluorine atom.[7,44,75] In Sarin, a hydrogen bond to the sp^2–oxygen atom was found to be ~1.7 times stronger than to the sp^3–O atom.[7] This suggests that the majority of the binding would involve the sp^2–oxygen atom. The binding energy of the sp^2–O atom-silica dimer was calculated as 8.90 kcal/mol at the MP2/cc-pVTZ level.[75] These interactions are much stronger than the hydrogen bond present in the water dimer, roughly 5 kcal/mol. [81] This may be due to larger dipoles on the hydrogen bond acceptors and donors in the CWAs and silica than in water,[82] or dispersion forces between the agent and the surface increasing stabilization and therefore binding energy.

In the case of bidentate hydrogen bonding, the adsorbate accepts two hydrogen bonds. Bidentate binding may happen on high-silanol-density surfaces where hydroxyl groups are in

close proximity. Bidentate interactions can include one or two hydrogen-bond acceptors on the adsorbate.[7,67,44] The majority of bidentate binding occurs through two bonds to the sp^2–oxygen, but can occur through the sp^2– and sp^3–oxygen atoms, or the sp^3–O and halogen atom.[43] Monodentate and bidentate binding of Sarin to silica is seen in Figure 6.

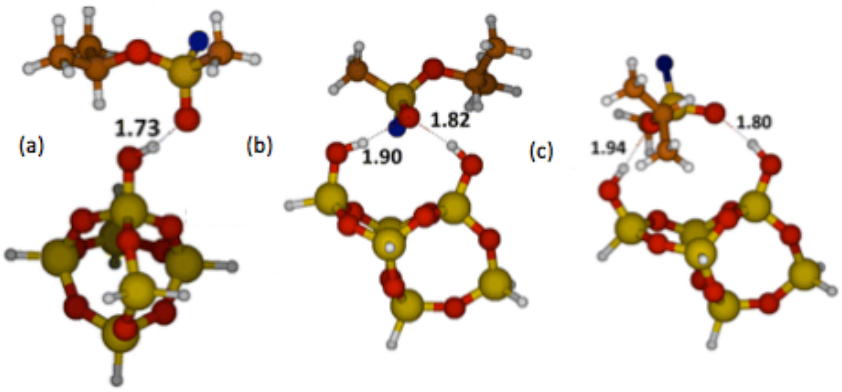

Figure 6. The (a) monodentate binding and bidentate binding of Sarin to the silica cluster through (b) the sp^2-O or (c) the sp^2-O and sp^3-O with the hydrogen bond distance in angstroms. Adapted with permission from Troya, et al.[7] Copyright 2013 American Chemical Society.

Less toxic mimics can be employed to investigate the functional portions of the active agents while reducing the risk to the experimentalist. These mimics must be tested to ensure that they are suitable replacements for the active agents.[43,83] For Sarin gas, common mimics include methyl dichlorophosphate (MDCP), dimethyl chlorophosphate (DMCP), trimethyl phosphate (TMP), diisopropyl methylphosphonate (DIMP), and dimethyl methylphosphonate (DMMP).[13,7,84] Figure 7 shows the mimics structures, which retain the P=O and P-O-R moieties of the parent molecule while altering other functionalities.

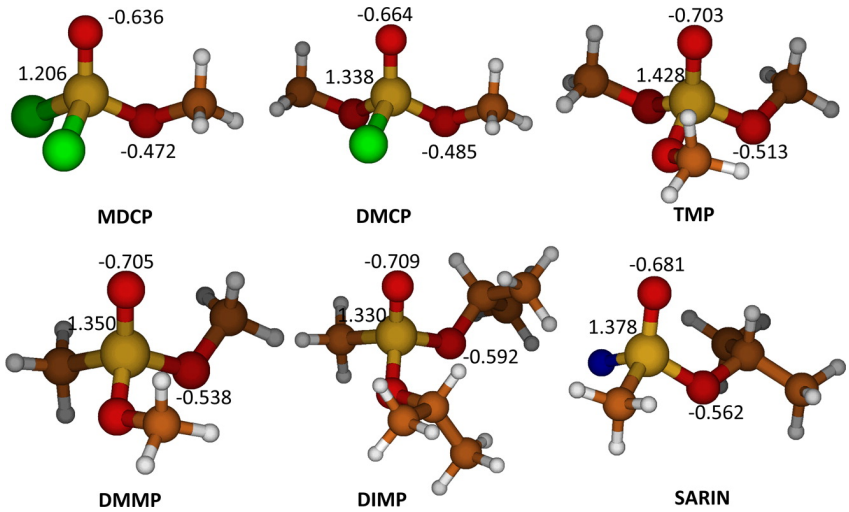

Figure 7. Sarin and its five mimics with Mulliken charges calculated at MP2/cc-pVQZ//6-31G*, where green is chlorine, blue is fluorine, yellow is phosphorous, tan is carbon, red is oxygen and hydrogen is white. Adapted with permission from Troya, et al.[7] Copyright 2013 American Chemical Society.

In a laboratory setting where safety is paramount, the suitability of these mimics is tested against data for the active agents. For example, the analysis of the Mulliken charges, or calculated atomic charges, for the sp^2 hybridized oxygen atoms shows that the charge on the Sarin gas sp^2-oxygen falls between those of DMCP and TMP at the MP2/cc-pVQZ//6-31G* level.[7] Comparing the Mulliken charges on the sp^2 oxygen to the measured activation energy of desorption shows a positive linear correlation (Figure 8), which suggests that the charge on the sp^2 hybridized oxygen atom may influence the strength of the adsorption to silica.

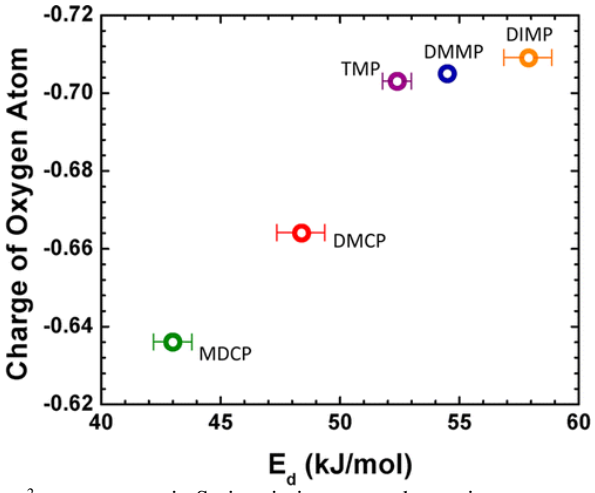

Figure 8. Mulliken charges on the sp^2 oxygen atom in Sarin mimics versus desorption energy on silica surface completed in UHV. Reprinted with permission from Wilmsmeyer, et al.[4] Copyright 2012. American Chemical Society.

In addition to nerve agents like Sarin and Soman, blister agents, such as mustard gas (HD), also interact with organic,[84,85] metal,[12] and metal oxide surfaces.[13,69,86] While the kinetics of diffusion and reduction of these gases on surfaces are well studied,[87] the interaction mechanism is not as thoroughly understood. In a paper by Kanyi et al.,[68] the interaction of HD and zeolites was studied. It was concluded that exposure of these metal-oxide surfaces to mustard gas and its simulants resulted in dehalogenation and much less toxic products.[88] A proposed mechanism for photocatalytic degradation of HD on TiO_2 included the formation of a metal-gas bond and radical bond breakage.[10,88] Investigation of HD and mimics, shown in Figure 9, on TiO_2/SiO_2 determined that adsorption on TiO_2 results in similar decomposition reactions, where Ti-O-adsorbate bonds were formed.[10,73] Similar results were seen on MgO.[77] Major decomposition products included ethylene, carbon monoxide, and sulfur dioxide. There was no evidence of decomposition on SiO_2. Instead, the experiment showed evidence that hydrogen bonds were formed between the sulfur and chlorine atoms and silanol surface groups.[71] These hydrogen-bonding interactions are the primary focus of this thesis.

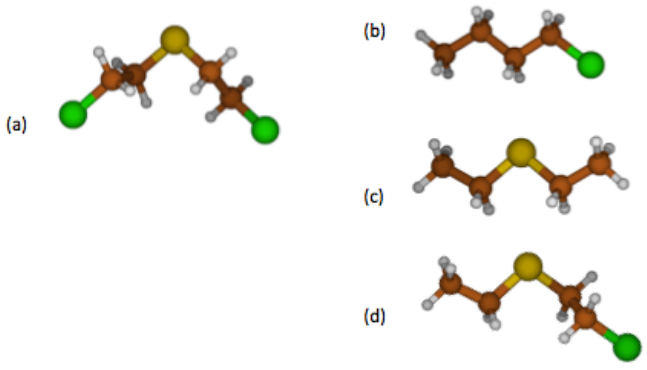

Figure 9. Structure of (a) mustard gas and its mimics (b) chlorobutane, (c) diethyl sulfide, and (d) 2-chloroethyl ethyl sulfide. Carbon is tan, hydrogen is white, chlorine is green and sulfur is yellow.

1.4. Application of Theory

Current computational research involves investigating the adsorption of CWAs to silica in an effort to probe the interaction of these adsorbates with a common surface. In the calculations, amorphous silica surfaces are approximated with a single silanol molecule or by a cluster. Use of a single hydrogen-bond donor on the surface excludes bidentate binding, which may be part of future research. Previous work[4,7,29,44,46,75] has successfully helped interpret of organophosphorous agents to silica. Ongoing research focuses on mustard gas and its mimics.

The mimics of mustard gas used in calculations and experiments are chloroalkanes, diethyl sulfide (DES), and 2-chloroethylethyl sulfide (2-CEES). These mimics were chosen to isolate binding domains and to determine how the interaction potential changes with the chemical structure of the adsorbate. The mimics were characterized using electronic structure calculations with the Gaussian 09 software[89] and are shown in Figure 9.

Investigating the interactions at gas-surface interfaces requires in-depth knowledge of the chemical and physical structure of both the surface and adsorbate molecule. This can be accomplished through experimental methods including IR and TPD. The mechanism of the adsorption can be determined through theoretical methods and supported by experimental evidence. The interactions of these toxic gases and their mimics with common materials such as silica can be probed safely using theoretical methods.

Chapter 2- Theoretical Basis and Methods

2.1. Theoretical Methods

Quantum mechanical theory determines atomic and molecular properties by solving the Schrödinger equation. Computational methods have been derived to solve the mathematics involved in the Schrödinger equation. These computational methods can help investigate the chemical properties, experimental observables, reactions, and mechanisms of a system. This includes systems that may not be easily obtainable or safe in a wet laboratory, such as chemical warfare agents.

Computational results, benchmarked by experimental evidence, can give new insight into a system.[90] The solution of the time-independent electronic Schrödinger equation can provide details about properties ranging from the energy of a given molecular structure to the frequencies of molecular vibrations and beyond.[91] In this work, the major focus is to understand the interaction and binding energy of CWAs on silica surfaces. The most accurate molecular energies are reached using methods that solve the electronic Schrödinger equation.

The Schrödinger equation describes how the observable properties can be predicted by knowing the nature of the wave function of the system. The Hamiltonian operator, $\hat{H}$, operates on a wave function, Ψ, to return a value of energy, E,[91] and is mathematically described as

$$\hat{H}\,\Psi = \mathrm{E}\,\Psi. \tag{11}$$

A wave function describes all the attributes of a particle in space.[92] The integral of a real wave function squared over a given volume provides the probability of finding that particle in that volume. The complicated nature of most wave functions requires simplification to be useful. The Born-Oppenheimer approximation suggests that a molecule's nuclear contribution to the kinetic energy can be separated from that of the electrons' contribution. This is the result of the protons'

mass, which is roughly 1800 times larger than of an electron, and therefore move much slower.[91] This approximation allows the wave function to be broken into two components, the nuclear term and the electronic term, described by

$$\Psi_{total} = \psi_{nuclear} + \psi_{electronic} \cdot \quad (12)$$

The Hamiltonian Operator contains kinetic and potential terms that describe the nuclei and electrons in a molecular system. The Hamiltonian Operator is written as

$$\hat{H} = \hat{T} + \hat{V} \quad (13)$$

where $\hat{T}$ is the kinetic term and $\hat{V}$ is the potential term. The kinetic term, dependent only on the mass and velocity of the particles in the system, is simpler than the potential. The potential energy term in a many electron system such as a molecule must account for all the attraction and repulsion of all charged particles. Due to these numerous interactions, the many-electron systems are not analytically solvable.[90] Using these concepts, various methods try to solve the Schrödinger equation mathematically for many electron systems.

2.1.1. Hartree Fock

The Hartree Fock method approximates many electron wave functions as a single Slater determinant of one-electron orbitals. A Slater determinant is a determinant of a matrix which accounts for the interchangeability of electrons in an orbital due to the anti-symmetry principle.[91] Use of Slater determinants accounts for exchange effects. Exchange effects are so called because the interchange of two electrons spin and position in a system affects the sign of the wave function.[93] This interchangeability arrives from the inability to distinguish electrons in a molecule. The one-electron Fock wave function is described as

$$\hat{F}_i \varphi_i(\vec{r}) = \varepsilon_i \varphi_i(\vec{r}) \quad (14)$$

where φ_i is the one electron wave function called the Hartree Fock orbital, ε_i is the eigenvalue for the energy, and $\widehat{F}_i$ is the one electron Fock operator.[94] The Fock operator can be written as

$$\widehat{F}_i = \widehat{h}_i + \sum_j [2\widehat{J}_j(i) - \widehat{K}_j(i)] \quad (15)$$

where $\hat{h}_i$ is the one-electron Hamiltonian, $J_j(i)$ is the Coulombic potential and $K_j(i)$ is the exchange interaction between electrons i and j.

The Hartree Fock method is an *ab initio* and self-consistent field method. *Ab initio*, or Latin for "from the beginning", is a method which does not require the input of experimentally determined fitting parameters. The nuclear positions, types of particles present, and a basis set to define the wave function are all that are needed to describe the system.[91] Basis sets are described in detail below. The self-consistent field method takes the initial input coordinates and creates an initial 'guess' density matrix that approximates the orbitals, which is then used to solve the secular Fock equations. The resulting orbital matrix is compared to the initial orbital matrix. If the differences between matrices are larger than the prescribed convergence criteria, the new matrix is used in place of the initial and the steps repeated. The iterative process is continued until the matrices reach consistency with the convergence criteria.[91]

While the Hartree Fock method does well at accounting for the exchange portion of the molecular picture, it ignores the electron correlation. The electron correlation, or instantaneous interaction between electrons in a system, is an important contribution to the system energy. A more accurate picture of the molecular energy includes electron correlations.

2.1.2. Density Functional Theory

Kohn and Sham[95] added a correction to the variational Hartree-Fock method to account for electron correlation. Density functional theory, or DFT, is another method for solving the

Schrödinger equation. Instead of describing the electrons in a system as a wave function, the system is initially described in terms of electron density, ρ.[91] The functional form for the energy as it depends on the uniform electron density is given as

$$E[\rho(\boldsymbol{r})] = T_{ni}[\rho(\boldsymbol{r})] + V_{ne}[\rho(\boldsymbol{r})] + V_{ee}[\rho(\boldsymbol{r})] + \Delta T[\rho(\boldsymbol{r})] + \Delta V_{ee}[\rho(\boldsymbol{r})] \tag{16}$$

where $\rho(\boldsymbol{r})$ is the electron density as a function of distance, T_{ni} is HF kinetic term, V_{ne} is potential energy between the nucleus and an electron, V_{ee} is the potential between two electrons, ΔT accounts for the change in kinetic energy due to the interacting nature of the electrons and ΔV_{ee} is a correction for the non-classical potential due to electron-electron repulsion. The last two terms give rise to the exchange and correlation corrections to the energy. The energy of the exchange and correlation accounts for all electron repulsion in a fully interacting system and is expressed as

$$E_{xc}[\rho(\boldsymbol{r})] = \Delta T[\rho(\boldsymbol{r})] + \Delta V_{ee}[\rho(\boldsymbol{r})] = \int \rho(\boldsymbol{r})\varepsilon_{xc}[\rho(\boldsymbol{r})]d\boldsymbol{r} \tag{17}$$

where ε_{xc} is the sum of individual exchange and correlation contributions for each electron. [91] The energy of just the exchange is written as

$$\varepsilon_x[\rho(\boldsymbol{r})] = -\frac{9\alpha}{8}\left(\frac{3}{\pi}\right)^{\frac{1}{3}}\rho^{\frac{1}{3}}(\boldsymbol{r}) \tag{18}$$

where α is the Slater exchange coefficient and the energy of the correlation is written as

$$\varepsilon_c^i(r_s) = \frac{A}{2}\left[\ln\frac{r_s}{r_s + b\sqrt{r_s} + c} + \frac{2b}{\sqrt{4c-b^2}}\tan^{-1}\left(\frac{\sqrt{4c-b^2}}{2\sqrt{r_s}+b}\right) - \frac{bx_0}{x_0^2 + bx_0 + c}\left(\ln\left[\frac{\left(\sqrt{r_s}-x_0\right)^2}{r_s + b\sqrt{r_s} + b}\right] + \frac{2(b+2x_0)}{\sqrt{4c-b^2}}\tan^{-1}\left(\frac{\sqrt{4c-b^2}}{2\sqrt{r_s}+b}\right)\right)\right] \tag{19}$$

where A, b, c, and x are fitting parameters and r_s is the effective radius.[96] The model above is only applicable for uniform electron densities, not found in most systems. For non-homogenous systems, DFT would give an exact molecular energy picture if the exact density functional were

known. In order to account for the inhomogeneity of the electron density in a molecule, additional approximations are used. These include local density approximations (LDAs) and general gradient approximations (GGAs).

LDAs calculate the correlation energy at a position as the function of the density at the point. This requires, however, that the densities are uniform over all space. This is not consistent with known orbital boundaries, whose density is inhomogeneous and taper off at large distances from the nucleus. GGAs correct for asymptotic long-range electron densities.[91]

Local spin density approximations (LSDAs) are required for open-shell systems that incorporate spin polarization. The energy of electron exchange is then expressed as

$$E_{xc}^{LSDA}[\rho_\alpha, \rho_\beta] = \int p(r)\varepsilon_{xc}(\rho_\alpha, \rho_\beta)dr \tag{20}$$

where ρ_α and ρ_β are the electron densities of electrons with α and β spin, respectively.[97]

DFT calculations include corrections for the correlation to the Hartree-Fock method and scale as N^3, where N is the number of basis functions and is two orders of magnitude faster scaling than MP2 with system size.[91] Many density functionals exist that include additional improvements to obtain more accurate results for a variety of systems. The functionals chosen for this project were B3LYP, B97D, and wB97XD. Some of these functionals were found to be particularly useful when describing the interactions between CWA and silica surface models.

B3LYP

The B3LYP density functional method is a hybrid functional that is commonly used in computational work and has broad applications.[98] In this research, B3LYP was initially used. B3 indicates the use of the Becke 3 parameter functional, which weights the contributions of exchange and correlation energies from the Becke 88 density functional method,[99] LSDA, HF,

and the GGA named after Lee, Yang, and Parr (LYP).[100] The equation for the B3LYP exchange and correlation energy is

$$E_{xc}^{B3LYP} = (1-a)E_x^{LSDA} + aE_x^{HF} + b\Delta E_x^B + (1-c)E_c^{LSDA} + cE_c^{LYP} \quad (21)$$

where a, b, and c are equal to 0.20, 0.72, and 0.81, respectively. These parameters were empirically chosen. The LYP GGA functional contains four additional fitting parameters, fit to Helium data. The LYP correlation energy takes the form

$$E_c = -4a \int \frac{\rho_2^{HF}(r,r)}{\rho(r)} \left(\frac{1 + b\rho(r)^{-8/3}[\nabla_s^2 \rho_2^{HF}(r,s)]_{s=0} e^{-cp^{-\frac{1}{3}}(r)}}{1 + d\rho(r)^{-1/3}} \right) dr \quad (22)$$

where ρ_2^{HF} is the second-order Hartree Fock density matrix and a, b, c, and d are equal 0.049, 0.132, 0.2533, and 0.329, respectively.[101] The Lee, Yang, and Parr corrections account for self-interaction error, or the inclusion of the interaction of one electron with itself.[96]

B97D

The B97D functional was selected due to its treatment of long-range dispersion interactions, which are present in the CWA-surface system.[102] B97D has proven to consistently account for van der Waals interactions as a result of a corrected gradient functional and the inclusion of an empirical dispersion term.[103] B97D calculates the energy of a system including dispersion interactions, E_{DFT-D}, as

$$E_{DFT-D} = E_{KS-DFT} + E_{disp} \quad (23)$$

which includes the Kohn-Sham energy, E_{KS-DFT}, and the energy dispersion interactions, E_{disp}. The energy of the dispersion interaction is then calculated as

$$E_{disp} = -s_6 \sum_{i=1}^{N_{at}-1} \sum_{i=j+1}^{N_{at}} \frac{C_6^{ij}}{R_{ij}^6} f_{dmp}(R_{ij}) \quad (24)$$

where s_6 is a scaling factor, C_6^{ij} is the dispersion coefficient for the atoms i and j, R_{ij}^6 is the inter-atomic distance between atoms i and j, and $f_{dmp}(R_{ij})$ is a damping function. The damping function's form is

$$f_{dmp}(R_{ij}) = \frac{1}{1 + e^{-d\left(\frac{R_{ij}}{R_r} - 1\right)}} \tag{25}$$

where R_r is the sum of the van der Waals radii for atoms i and j. This form of the damping function corrects the potential energy surface at small atomic distances. This can be seen in Figure 10.

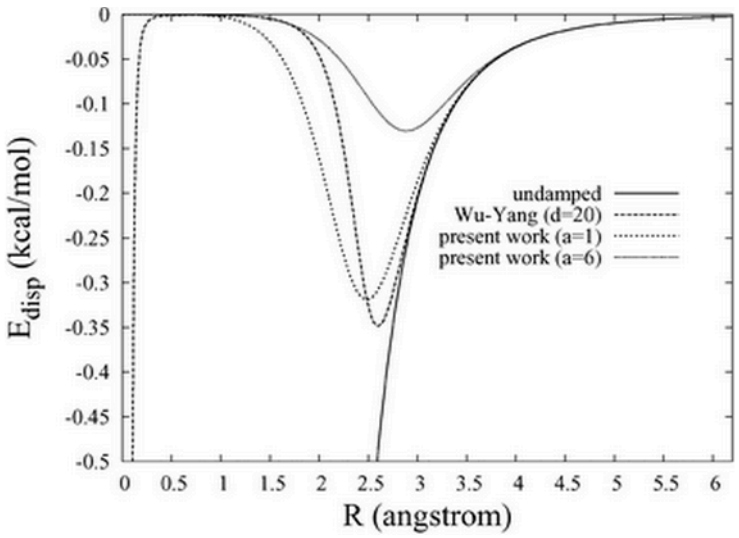

Figure 10. Dispersion energy diagram of a Neon dimer where the undamped function is an example of B3LYP, the Wu-Yang(d=20) is an example of B97D, and the present work is an example of wB97XD where the non-linear parameter has been varied. Reproduced Chai, et al. [104] with permission of The Royal Society of Chemistry.

ωB97X-D

ωB97X-D is similar to B97D and includes corrections for long-range dispersion forces. The damping function takes on a different form

$$f_{dmp}(R_{ij}) = \frac{1}{1 + a(\frac{R_{ij}}{R_r})^{-12}} \tag{26}$$

where a is non-linear parameter for the control of dispersion interaction strength.[104] This correction is different from that in the B97D functional because it corrects for the divergence seen at smaller inter-atomic distances, as seen in Figure 10.

For the chemical warfare agent and silica surface system, B97D and wB97XD were used to capture the dispersion forces present between the atoms of HD, 2-CEES, and DES and the oxygen atoms at the surface. The differences between B97D, ωB97X-D, and B3LYP results will be described in the Chapter 3.

2.1.3. Basis Sets

A basis set is a mathematical attempt to describe a molecular orbital in terms of functions. Within HF, the larger the basis set, the more comprehensive the approximation and the closer it is to approximating the HF limit. Beyond a hydrogen-like state, describing molecular orbitals as linear combinations of atomic orbitals or LCAOs becomes tedious.[91] Two types of orbitals, Slater-type orbitals (STOs) and Gaussian-type orbitals (GTOs), are typically used to describe molecular orbitals. STOs are more computationally expensive than GTOs. STOs have an exponential form of e^{-r} while GTOs have the Gaussian form of e^{-r^2}. The difference between the two types of orbitals can be seen in Figure 11. Linear combinations of primitive GTOs are used to approximate the radial shape of STOs. The linear combinations of GTOs are better representations of the cusp of the wave function at r=0, seen in Figure 11. The combinations are referred to as a contracted basis function and are sometimes given the form STO-*M*G, where *M* is the number of primitive Gaussians in the contracted function. Compromising accuracy and speed, the typical number utilized is three.

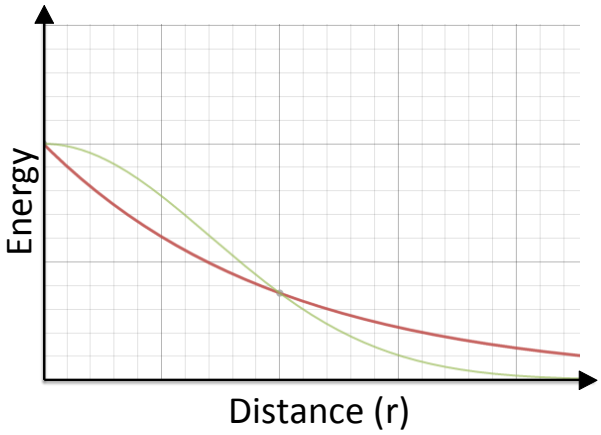

Figure 11. The shape of Slater-type orbital wave function in red and Gaussian-type orbital wave function in green.

Single-ζ, double-ζ, triple-ζ, and so forth are used to describe basis sets where there are one or more functions describing one orbital. Single-ζ would have one function, double-ζ would have two and so on. Additionally, split-valence refers to the treatment of core orbitals separately from the valence orbitals. The core orbitals can be described using a contracted Gaussian while the valence electrons may be described by multiple functions. This is logically and chemically sound, as the contracted and full core orbitals change very little in regards to the external chemical environment. An example of common nomenclature used for split-valence basis sets includes 6-311G, where the first number indicates the number of primitive Gaussians used to describe the core orbitals and the numbers after the hyphen describe the number of primitive Gaussians used to describe the valence orbitals. One number after the hyphen is a single-ζ, two represents a double-ζ, and so on. In the 6-311G example, the valence electrons are a linear combination of 3 functions, the first function being a linear combination of 3 GTOs, the second a single GTO, and the last also being a single GTO. Correlation consistent and polarized split valence multi-zeta basis sets are written as cc-pV*X*Z where *X* is D for double, T for triple, and so on. Correlation consistent basis sets include all the basis functions calculated by Hartree Fock theory and additional basis functions that account for single and double excitations from the state specified for the system, such as the ground state.[105] An example of this is in the cc-pVTZ basis

set for a ground state carbon atom, where an additional 4s, 3p, 2d and 1f functions are added to the those calculated by Hartree-Fock theory.[106]

Another type of function added to basis sets are polarization functions, shown as the 'p' in cc-pVTZ or as an asterisk (*) in 6-31G* notation. These functions help bridge the gap between atomic orbitals and basis sets for molecular orbitals. The polarization function adds an additional orbital one angular quantum number higher than that for the valence shell of the atom for which it is prescribed. This is equivalent to including p-orbitals on a hydrogen atom and a d-orbital on oxygen. To add additional accuracy, diffuse functions are utilized to characterize the electron density of loosely bound species. These functions are represented as a plus sign (+) as in 6-31+G* or as an abbreviation of the word augmented in aug-cc-pVTZ.

In an effort to approximate an infinitely large basis set, molecular energies can be extrapolated to the completed basis set limit. Dual-level calculations, where geometries optimized at a lower level of theory are using to obtain molecular energies at higher levels, were used in this research. B97D/6-31G** optimized geometries were used as input geometries for molecular energy MP2/cc-pVTZ and MP2/cc-pVQZ calculations. The correlation energy at the complete basis set limit, E_{CBS}^{corr}, can be calculated as a function of these molecular energies by the following equation

$$E_{CBS}^{corr} = \frac{3^{\beta}}{3^{\beta} - 2^{\beta}} E_3^{corr} - \frac{2^{\beta}}{3^{\beta} - 2^{\beta}} E_2^{corr} \tag{27}$$

where β is a fitting parameter with a value of 2.2 for MP2 calculations, and E_3^{corr} and E_2^{corr} refer to the MP2/cc-pVTZ and cc-pVQZ correlation energies, respectively.[107] This method was used in this research to calculate the energies of all complexes to the complete basis set limit. These basis sets and computational methods are the foundation for the molecular modeling of the electronic structure calculations in this research.

2.2. Applications and Job Types

Applying computational chemistry involves the implementation of many types of jobs of varying computational demand. Specifying a particular job type or series of job types and basis set returns detailed results, from molecular geometries to electrostatic potentials. Additional theoretical tools, such as dihedral scans, can be used to alter the job types to get further insight into the studied system.[109] In this research, the first step was the geometry optimization of all adsorbates and surfaces models.

2.2.1. Geometry Optimization

Geometry optimizations result in the conversion of an initial or guess geometry to an energy minimized geometry. The method used to conduct geometry optimizations in Gaussian 09[89] is "Berny's algorithm"[109] created by Bernard Schlegel.[110] An initial Hessian (H) matrix is constructed by determining of the force constants for the initial geometry. With the exception of the initial Hessian, the Hessian is normally computed as the second derivative of the electronic energy with respect to atomic position.[111]

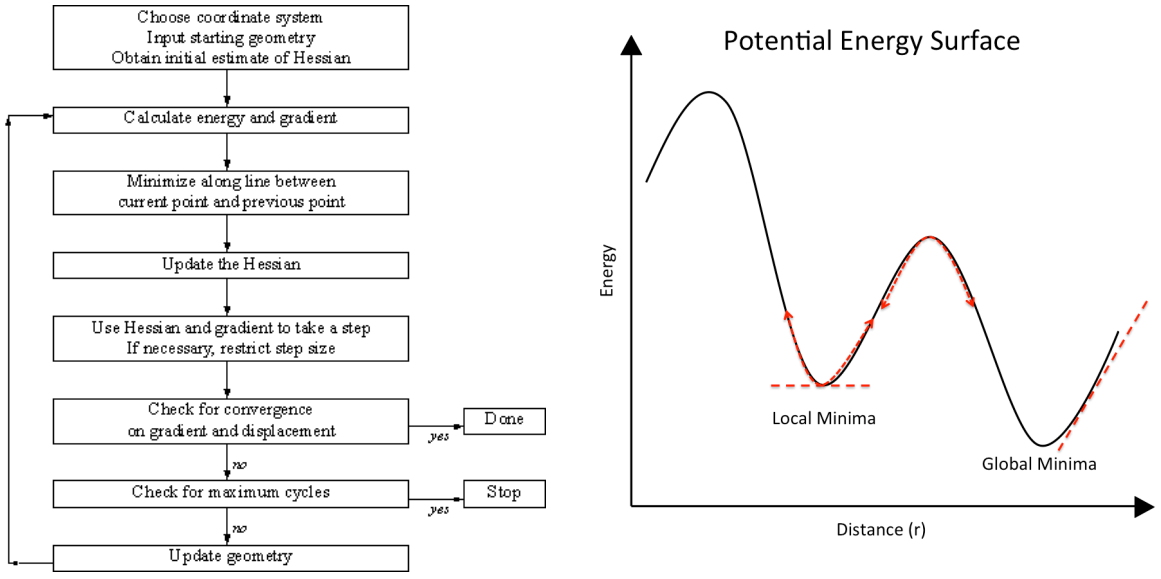

(a) (b)

Figure 12. (a) Optimization scheme used in Gaussian 09 based on Bernard Schlegel's algorithm. Adapted from B. Civalleri.[108] (b) Potential energy surface diagram where the straight red-dashed line indicates the slope of the line or the vibration at a point and the curved red dashed line indicates the vibrational direction from the center point.

This geometry optimization process is outlined in Figure 12(a) and continues until the atomic distances and changes in the Hessian matrix reach convergence with a set of arbitrary criteria. The new geometry is an energy minimum. In Figure 12(b), a model potential energy surface is shown. If an initial geometry guess is equivalent to a peak, the optimization occurs and the energy gradient decreases until the slope of the line is zero. The slope of the line, represented as a straight red-dashed line in Figure 12(b), is zero at minimum and maximum and non-zero at all other geometries and is analogous to the energy gradient.

A geometry optimization results in a minimum energy atomic conformation. In order to determine additional information, other calculations can be performed to the optimized geometry. Frequency calculations determine if the optimized geometry is a local minimum by determining the vibrational modes associated with the complex.

2.2.1.1. Frequency Calculations

In this work, when an optimized geometry is located, that geometry is used to solve for the force constants and vibrational modes. All the frequencies for this research are in the IR spectrum though Raman spectroscopy frequencies, and the intensities can also be calculated.[109] Frequency calculations begin with mass-weighting the Hessian matrix of an optimized geometry of system.[112] This mass weighted Hessian is then transformed into an internal coordinate system that includes information on the inertia and rotational axes of the system. The diagonalization of the Hessian matrix returns eigenvalues which are used as force constants. The non-mass weighted force constants, k_i, are converted to frequencies by the classical equation

$$\tilde{\nu}_i = \frac{1}{2\pi}\sqrt{\frac{k_i}{\mu_i}} \tag{28}$$

where $\tilde{\nu}_i$ is the frequency and μ_i is the reduced mass. The frequencies of the optimized structure of the system give additional insight into the system. If the system returns all positive values for frequencies, it is said to be in a local minimum on the potential energy surface. In Figure 12(b), this is seen as the bottom of the well. At the bottom of the well, all frequencies must be positive. If a single imaginary frequency is returned, the optimized geometry corresponds to a transition state. This is seen in Figure 12(b) as the top of the peak, where the curved dash line indicates an imaginary frequency. More than one imaginary frequency likely means that the returned geometry is a higher-ordered transition state or saddle point and additional optimization is needed. In this work, if an imaginary frequency was returned from the calculation, the geometry would be altered in the direction of the vibration and a new geometry optimization would be carried out.

2.2.2. Basis Set Superposition Error

In this research, the binding energy between the adsorbate and the surface model is calculated as the energy difference between the reactants and the product complex. In the case of HD on a silica cluster model, the energy of adsorption (E_{ads}) would be calculated as

$$E_{ads} = E_{complex} - \left(E_{adsorbate} + E_{surface}\right) \tag{29}$$

where $E_{complex}$ is the electronic energy of the adsorbate/surface complex, $E_{adsorbate}$ is the energy of the adsorbate and $E_{surface}$ is the energy of surface. This approach, however, neglects basis set superposition error or BSSE.

BSSE is the result of a computational method in which a molecule 'borrows' basis functions from atoms in a neighboring molecule in an effort to more accurately describe an atom with a larger basis set. This delocalization of basis functions affects the $E_{complex}$ term, since the intermolecular borrowing of orbitals is not an accurate description of the system for a particular

basis set. To arrive at a more accurate $E_{complex}$ term for a particular basis set, the counterpoise corrected method for calculating BSSE is employed in this research.[113]

The counterpoise corrected interaction energy of the complex, ΔE_{int}, could be calculated as

$$\Delta E_{int} = E_{A-B} - E_A - E_B - \Delta E_c \quad (30)$$

where E_{A-B} is the complex of reactants A and B with delocalized basis sets, E_A and E_B are the energies of the reactants A and B at infinite separation, and ΔE_c is the counterpoise correction.[114] The counterpoise correction is computed as

$$\Delta E_c = (E_A^+ - E_A) + (E_B^+ - E_B) \quad (31)$$

where the E_A^+ and E_B^+ are the energies of reactants A and B, respectively, where the delocalization of the basis sets has been allowed in the calculation of the reactant energy.[115] This counterpoise corrected method to remove BSSE was selected for this research as it has been shown to more accurately calculate the binding energy in hydrogen bonding systems.[116]

2.2.3. Population Analysis

The molecular orbitals and charge density assigned to each reactant and product complex are analyzed using full population analysis.[117] Mulliken's method for population analysis was used to assign electronic and charge density to each atom in each molecule studied.

Mulliken Charge Analysis

Mulliken determined that partial charges could be assigned to a single atom by a linear combination of atomic orbitals (LCAO).[118] These LCAOs can then be used to describe the molecular orbitals. In order to obtain the partial charge on an atom in a molecule, the electronic charge population of that atom must be determined. The population is dependent, $\boldsymbol{P}_{\alpha\beta}(r)$, on the

basis set, α, the atomic orbital, β, and the distance from the nucleus, r. Knowing the electronic charge population and the atomic number, Z_a, the partial charge can be calculated as

$$q_A = Z_a - \int \boldsymbol{P}_{\alpha\beta}(r)\, dr. \tag{32}$$

Partial charges are used in this research to qualitatively discuss observed trends. Additionally, the population of specified molecular orbitals can be calculated using LCAOs. The charge and orbital densities can be used in conjunction with Molecular Orbital (MO) theory to give further insight into the system.

2.2.3.1. Molecular Orbital Theory

Molecular Orbital theory is an expansion of atomic orbital theory where atomic orbitals of neighboring atoms overlap to form new MOs. The MOs give a picture of the orbital shape, energy, and charge density.[119] In this work, the MOs were calculated and used to explain trends in hydroxyl-stretching modes.

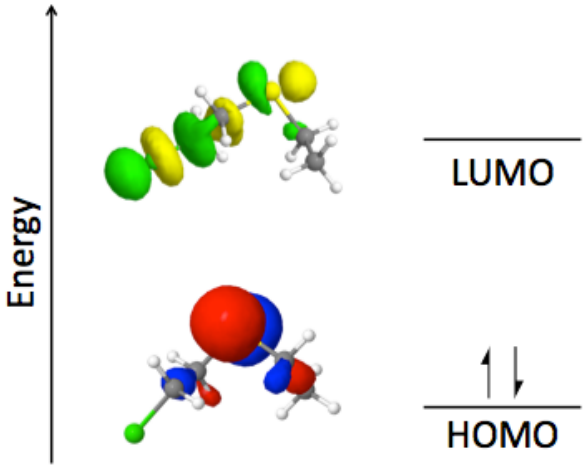

Figure 13. MO diagram of the HOMO and LUMO of 2-CEES determined at B97D/6-31G**. In this figure, chlorine atoms are green, carbon atoms are grey, hydrogen atoms are white, and sulfur atoms are yellow.

Interactions primarily occur between frontier orbitals of molecules.[120] Although other occupied and unoccupied orbitals exist, the frontier orbitals include the highest occupied molecular orbital (HOMO) and lowest unoccupied molecular orbital (LUMO). In Figure 13, the

HOMO and LUMO of 2-CEES were determined at B97D/6-31G**. Two possible hydrogen bonding accepting domains exist in 2-CEES, the lone pair electrons on the chlorine and sulfur atoms. In the HOMO, there is large orbital density around the sulfur atom and very little to no orbital density around the chlorine atom. The opposite is true in the LUMO. This information on the frontier orbitals will be used later to discuss the differences between the hydrogen bonding domains of 2-CEES and HD.

In addition to the location of orbital density, the orbital energy plays a major role in interaction strength. In some intermolecular interactions, the HOMO of one molecule will donate electron density into the LUMO of another molecule. This donation requires that the orbitals be close enough in energy to share electrons. The strength of this interaction is proportional to the orbital overlap and indirectly proportional to the difference in orbital energy.[121] Therefore, if the difference in orbital energy of the HOMO and LUMO is small, the interaction energy should be large, assuming sufficient orbital overlap. These ideas and molecular orbitals allow for the drawing of qualitative conclusions about interaction energies.

Chapter 3- Results and Discussion

The adsorption of sulfur mustard and its mimics to amorphous silica was studied using computational methods. The adsorbate conformation, adsorbate-surface structure, binding energy, vibrational information, and molecular orbital energies were determined for each mimic and surface system in order to develop a comprehensive understanding of the hydrogen binding interaction characteristics, include electrostatics and charge transfer contributions.

3.1. Results

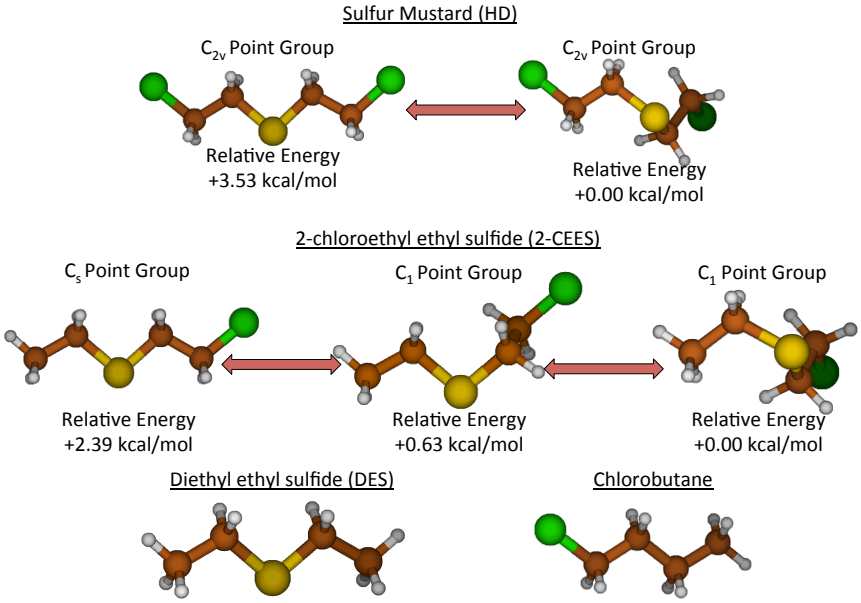

Figure 14. Conformers of HD and 2-CEES, including their relative energies in kcal/mol and the structures of DES and chlorobutane calculated at the B97D/6-31G** level of theory.

Sulfur mustard has two possible hydrogen-bond acceptors that can interact with the hydroxyl groups of a silica surface, the chlorine atoms and the sulfur atom. The traditional portrayal of HD, a C_{2v} point group molecule, has the chlorine atoms in isoelectronic environments. A more stable confirmation of HD was discovered serendipitously while investigating the traditional an d higher energy C_{2v} conformer to a silica cluster. This lower energy conformer also has the chlorine atoms in identical environments and has C_{2v} symmetry. It was determined at B97D/6-31G** that the bent C_{2v} conformer was 3.53 kcal/mol lower in

energy than the planar C_{2v} version of the molecule. This new conformer was called the 2-gauche conformer, due to the gauche defect around a carbon-sulfur bond when viewed as a Newman projection. These conformers are illustrated in Figure 14.

The same 2-gauche defect in the 2-CEES molecule results in an energy that is 2.93 kcal/mol lower than the planar conformation. Additionally, a third stable conformer was located during the investigation of the energetics of this molecule. The lowest energy conformer, seen on the left side of Figure 14, was named to the 2-gauche 2-CEES molecule due to the gauche defect around the sulfur-carbon bond. The third stable conformer, seen in the middle, was named the gauche conformer, due to the defect seen around the carbon-carbon bond of the 2-chloroethyl group that neighbors the sulfur. This conformer was determined to be 0.63 kcal/mol higher in energy than that of 2-gauche 2-CEES molecule. The 2-gauche and gauche defects were imposed upon the DES molecule but were determined to be unstable. The lowest energy conformers of each adsorbate were used in all dimer calculations. With an understanding of the energy and adsorbate conformations, various silica models were chosen to maximize computational efficiency while retaining an adequate representation of the surface.

3.1.1. Silica and DES

Multiple surface models were utilized extensively in this research. The first model used was the single silanol molecule ($H_3SiO—H$) in Figure 15a, which was primarily used to capture hydrogen-bonding energy trends. Next, a cluster model was used as more extensive representation of the surface and to capture dispersion forces, or instanteous dipole-induced dipole interactions, between the adsorbate and the surface. Two possible conformers of this surface cluster model were also determined. The two conformers arise from the position of the hydroxyl group relative to the surface. These conformers can be seen in Figure 15(b) and (c).

The cluster conformation was taken into consideration when calculating binding energies, as the cluster in 15(b) is 0.1 kcal/mol higher in energy than the other conformer at MP2/CBS//B97D/6-31G**. Finally, the extended cluster in 15(d) was constructed to capture additional dispersion interactions that attempt to model an expended silica surface.

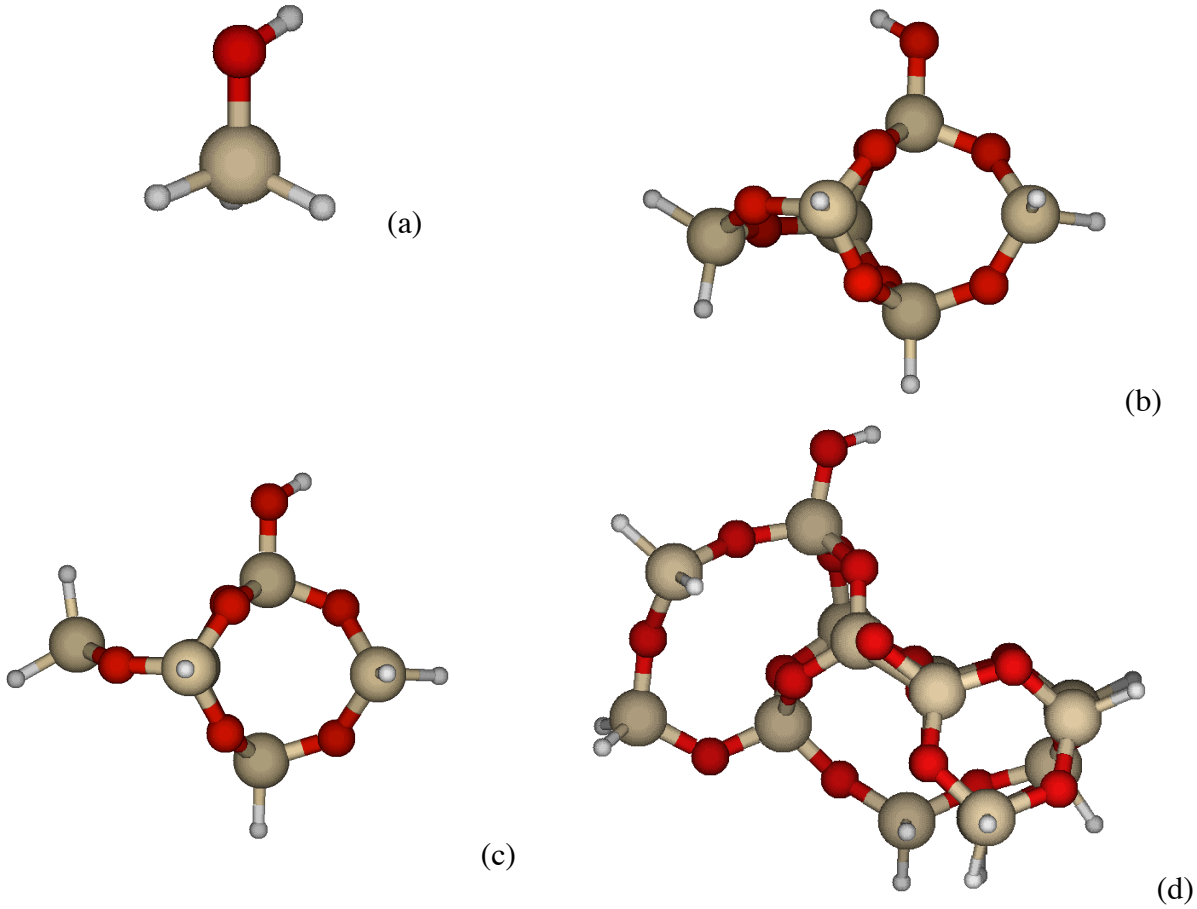

Figure 15. The surface models used in this research, including the (a) gas-phase silanol molecule, the (b) and (c) conformers of the cluster, and the (d) extended cluster. All optimized geometries were calculated at the B97D/6-31G** level of theory.

In addition to the two conformers, the cluster model of the surface was not symmetrical. This asymmetry created multiple electronic environments with which the adsorbates could interact. The study of each adsorbate on the surface was conducted via geometry optimization calculations. In Figure 16, multiple stable conformations of DES with the cluster are shown with their energies relative to the lowest energy conformer.

Figure 16 indicates how the conformation of DES with respect to the surface affects the binding energy of the complex. The DES-cluster complex has the lowest energy when DES has the most opportunities to participate in dispersion interactions with the surface. This is evident in Figure 16E, where the entire DES molecule is located in close proximity to the cluster. In contrast, the conformation in Figure 16A includes a complex where an ethyl moiety of DES is oriented away from the cluster. The orientation of this ethyl moiety does not allow for large dispersion interactions with the cluster and raises the energy of the complex. This reasoning can be used to explain all of the relative energies in Figure 16. The binding energy was determined for various adsorbate-complex conformers and the lowest energy complex was located.

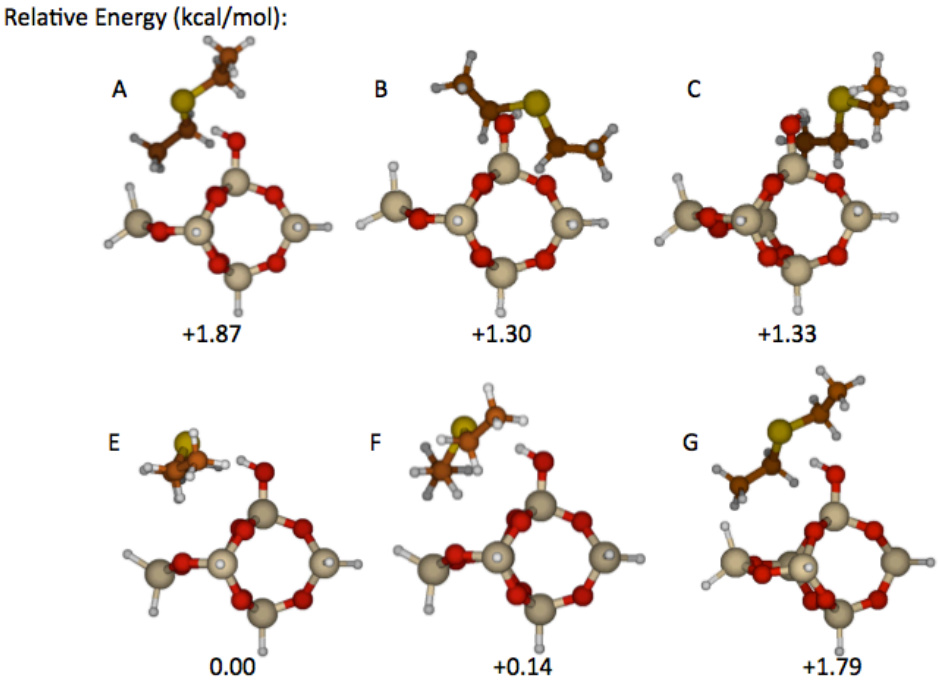

Figure 16. Complexes between the surface cluster model and DES where relative energies are calculated at the B97D/6-31G** level of theory.

3.1.2. Binding Energy

Using the information about multiple conformers and surface features, the lowest energy conformations of the adsorbate and surface model were employed to calculate the binding

energy. The counterpoise corrected binding energies of all surface-adsorbate complexes were calculated using Equations 29 and 30.

3.1.2.1. Chloroalkanes

Chlorobutane, a mimic of HD, has multiple methylene units. The contribution of these methylene units to the binding energy was studied by the successive addition or deletion of a methylene unit from chlorobutane. Therefore, chlorethane, chloropropane, chlorobutane, and chloropentane were hydrogen bonded to the surface by their chlorine atom. The energies of these chloroalkane-silica complexes are listed in Table 2. Initially, the B3LYP hybrid density functional was used with a 6-31G** basis set. However, the B3LYP/6-31G** values do not show a change in binding energy that is dependent on the number of methylene units. This result was unexpected, as additional methylene units increase the possibility for dispersion interactions with the silica surface. Two functionals that include empirical functions that account for long-range dispersion forces were then employed to capture the dispersion interactions. The B97D and w-B97XD functionals both result in an increase in the counterpoise corrected binding energies between chloroethane and chloropentane. The increase in energy did not increase linearly with methylene unit, as predicted by experiment,[27] but begins to diminish after chloropropane. This non-linearity has been attributed to the finite structure of the cluster, which cannot capture all the dispersion interactions of longer alkyl chains. Therefore, an extended cluster was constructed in an effort to capture these interactions and the results are shown at B97D/6-31G** level of theory in Table 2. These results are discussed later.

Table 2. The counterpoise corrected binding energies in kcal/mol calculated at B3LYP, B97D, and w-B97XD levels of theory with 6-31G** basis sets for the chloroalkane series on the silanol and small cluster models. The lengths of the hydrogen bonds are calculated in angstroms at each level of theory.

Counterpoise Corrected Binding Energy (kcal/mol) and Hydrogen Bond Lengths							
Silica Model	Adsorbate	B3LYP/6-31G**		B97D/6-31G**		w-B97XD/6-31G**	
		Binding Energy	Bond Length (Å)	Binding Energy	Bond Length (Å)	Binding Energy	Bond Length (Å)
Silanol	Chloroethane	3.00	2.37	4.71	2.51	4.60	2.53
	Chloropropane	3.01	2.46	4.98	2.55	4.93	2.54
	Chlorobutane	3.00	2.45	5.10	2.54	5.08	2.53
	Chloropentane	3.02	2.46	5.13	2.56	5.08	2.56
Cluster	Chloroethane	3.22	2.39	6.59	2.35	6.43	2.43
	Chloropropane	3.22	2.37	7.86	2.36	7.70	2.35
	Chlorobutane	3.27	2.38	8.47	2.38	8.29	2.36
	Chloropentane	2.87	2.39	8.88	2.38	8.73	2.36
Extended Cluster	Chloroethane	-	-	10.44	2.47	-	-
	Chloropropane	-	-	10.90	2.39	-	-
	Chlorobutane	-	-	11.65	2.33	-	-
	Chloropentane	-	-	11.55	2.35	-	-

The resultant lowest energy conformations of the chloroalkane series, calculated at B97D/6-31G** and wB97XD/6-31G**, are shown in Figure 17(a) and (b). The optimized geometries determined by the different methods are almost identical for similar systems. The similar complexes result in similar hydrogen bond lengths, which are included in Table 2. This suggests that the hydrogen bond energy remains relatively constant and the increase in dispersion interactions between the adsorbates and the surface increases the binding energy.

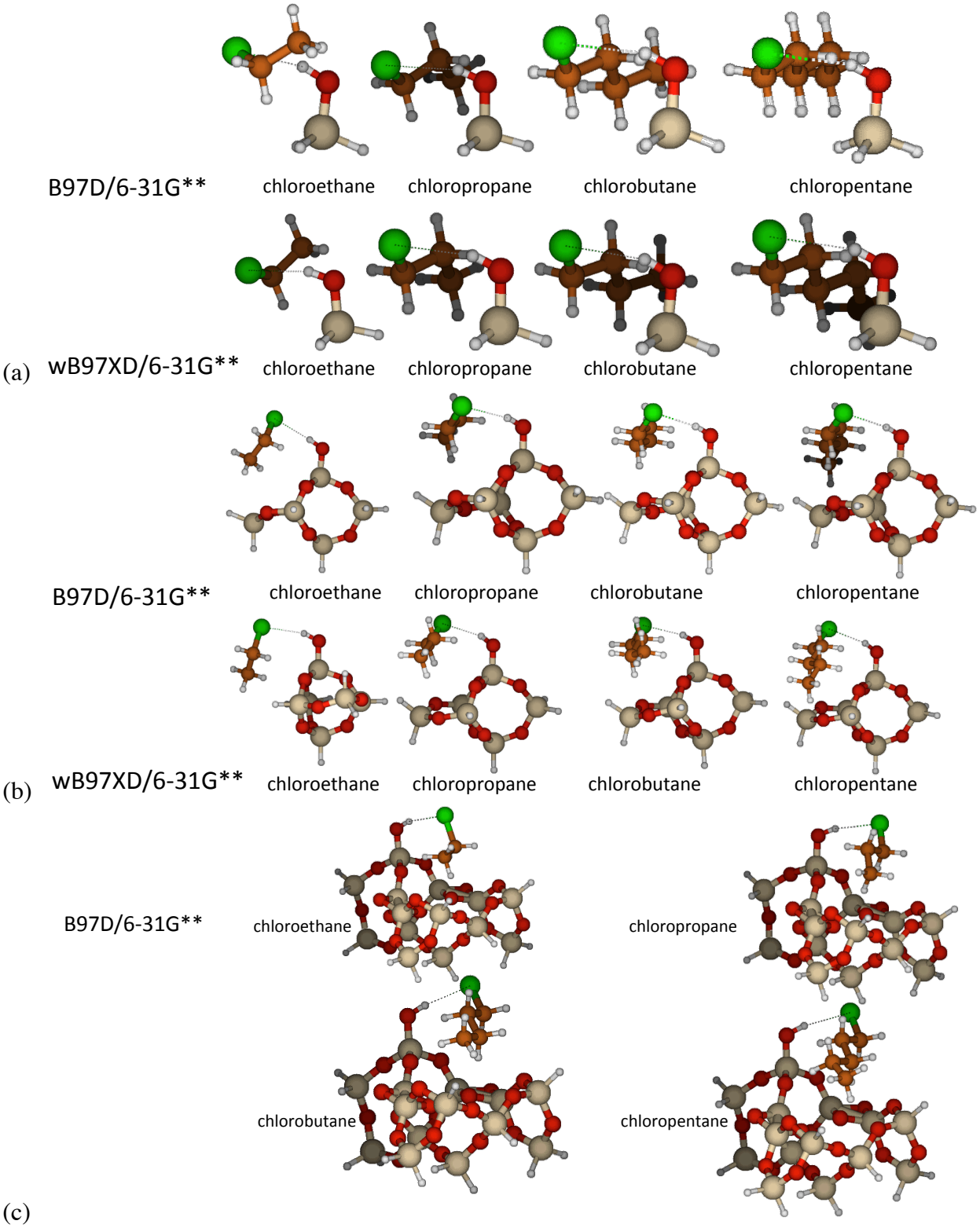

Figure 17. Lowest energy adsorption complexes of the chloroalkane series on (a)silanol, (b)a silica cluster and on the(c) extended cluster. The level of theory is indicated.

The study of the chloroalkane series concluded that the B3LYP functional was not able to capture the dispersion interactions of the chloroalkane series. The binding energy values did not change with additional methylene groups, as predicted in experiment, when the B3LYP functional was used. However, the B97D and wB97XD functionals captured the dispersion forces in these systems and provided near identical results with a basis set of 6-31G**. The chloroalkane series was benchmarked at MP2/CBS//B97D/6-31G**, which is discussed in Section 3.2.1. The lowest energy conformers of HD, 2-CEES, and DES used the B97D/6-31G** level of theory.

3.1.2.1. Mustard Gas and Mimics

Sulfur mustard and its mimics contain one or more hydrogen bond accepting moieties in addition to multiple methylene units. Each hydrogen bond acceptor was investigated for every mimic of HD. The optimized geometries of the agent and mimics to the gas-phase silanol and cluster are detailed in Figure 18. The hydrogen bond length in units of angstroms is specified for each mimic. Additionally, the hydrogen bond acceptor is noted in parentheses. Figure 18 indicates that, for the same adsorbate, the hydrogen bonds lengths when sulfur is the hydrogen bond acceptor are shorter than when chlorine is the acceptor in all cases. It is also the case that all hydrogen bond lengths are shorter when the surface model is the small cluster than when the model is the gas-phase silanol. The counterpoise corrected binding energies for these complexes are reported in Table 3.

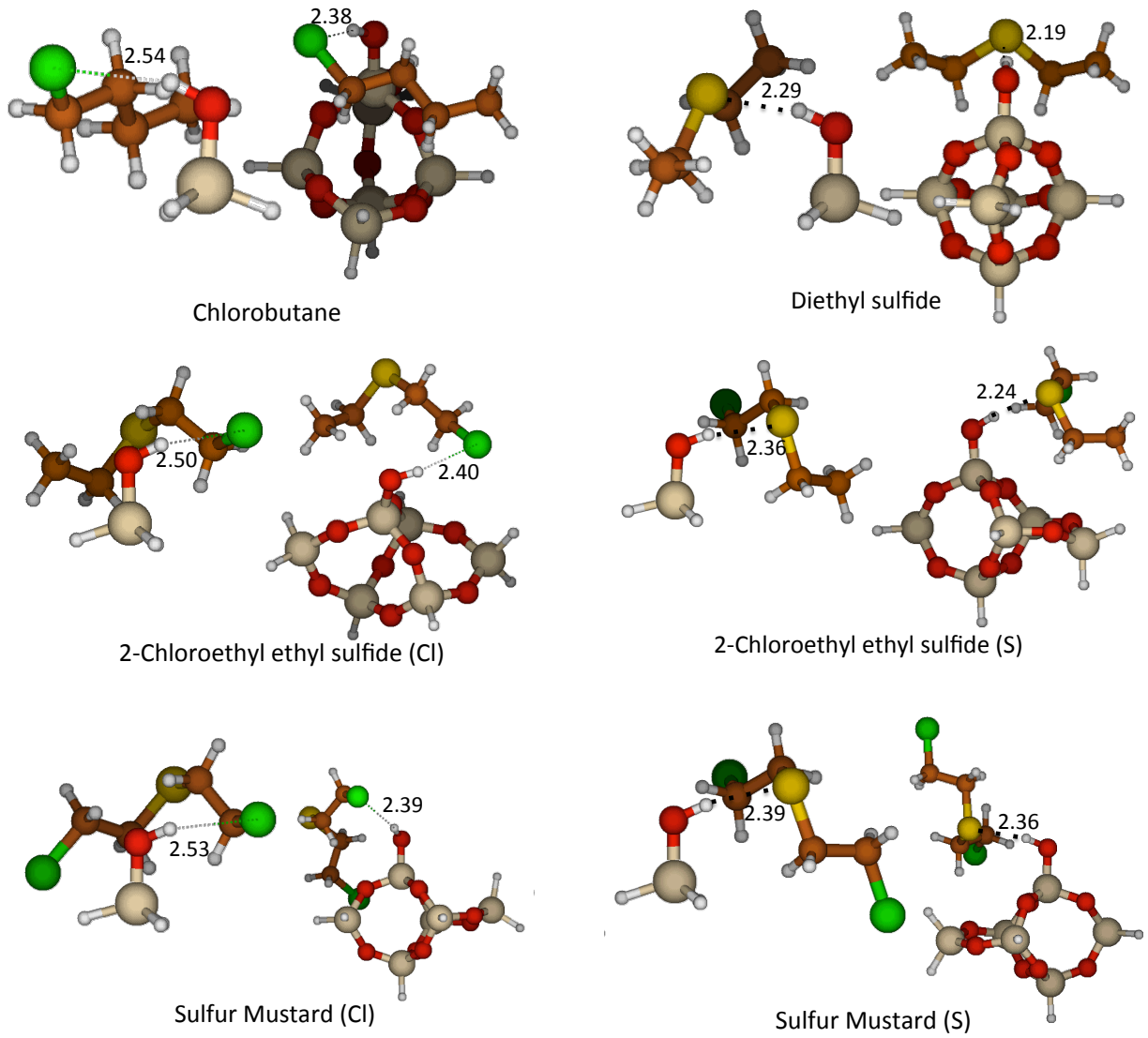

Figure 18. Optimized geometries of sulfur mustard and its mimics. The hydrogen bond acceptor is noted in parenthesis. The hydrogen bond distance is shown in angstroms (Å).

The MP2/CBS//B97D/6-31G** energies in Table 3 show that the adsorption of the mimics and agent to the gas phase silanol surface model resulted in lower binding energies than when binding occurred to the cluster. The longer hydrogen bond lengths in the silanol models from Figure 18 predicted this outcome, as the longer bonds indicate small binding energies. Additionally, the binding energies of each adsorbate where sulfur is the hydrogen bond acceptor are larger than when chlorine is the acceptor. The exception to this is in HD adsorption to gas phase silanol and to the cluster. The differences in the cluster complex binding energies that arise

from the two hydrogen bond acceptors in HD are relatively close and are considered to be the same in comparison to the other adsorbates. The differences in binding energies will be discussed in detail later.

Table 3. The counterpoise corrected binding energies in kcal/mol for sulfur mustard and its mimics at MP2/CBS//B97D/6-31G**. The hydrogen bond acceptor is noted in the parenthesis.

Binding Energies for Agent and Silanol at MP2/CBS//B97D/6-31G**			
Agent (Donor)	Binding Energy (kcal/mol)	Agent (Donor)	Binding Energy (kcal/mol)
Sulfur Mustard (Cl)	6.91	Sulfur Mustard (S)	5.62
2-CEES (Cl)	6.16	2-CEES (S)	6.49
Chlorobutane	4.87	DES	7.25
Binding Energies for Agent and Cluster at MP2/CBS//B97D/6-31G**			
Sulfur Mustard (Cl)	9.29	Sulfur Mustard (S)	8.60
2-CEES (Cl)	8.19	2-CEES (S)	9.40
Chlorobutane	7.56	DES	10.56

3.1.3. Vibrational Analysis

The vibrational analysis of all surface models, adsorbate, and complexes were performed at the B97D/6-31G** level without the use of scaling factors. The lack of imaginary frequencies ensured that all optimized geometries were indeed stable minima and not transition states. The primary focus of the vibrational analysis was to track changes to the frequency of the hydroxyl-stretching mode of the surface models upon binding. The IR active hydroxyl-stretching mode is measured experimentally.[27] Both the theoretical predictions and experimental data for the hydroxyl-stretching mode frequency develop a more detailed picture of the binding interaction, giving insight into the charge transfer component of the binding. The frequency shift of the hydroxyl-stretching mode was recorded for all adsorbates.

3.1.3.1. Hydroxyl Stretching Mode Shifts

The frequency of gas-phase silanol surface ‘free’ hydroxyl stretching mode is 3810 cm^{-1} at the B97D/6-31G** level of theory. The two conformers of the silica cluster had ‘free’

hydroxyl-stretching modes of 3829 and 3826 cm^{-1} using the same level of theory. The difference between the free and bound states, $\Delta\nu$, is also calculated. These results are presented in Table 4.

Table 4. Hydroxyl-stretching mode frequencies of all adsorbate-surface complexes in cm^{-1}. All values calculated at B97D/6-31G**.

Gas-phase Silanol and Adsorbate Values							
Agent	Free Stretching Mode (cm^{-1})	Bound Stretching Mode (cm^{-1})	$\Delta\nu$ (cm^{-1})	Agent	Free Stretching Mode (cm^{-1})	Bound Stretching Mode (cm^{-1})	$\Delta\nu$ (cm^{-1})
Mustard (Cl)	3810	3722	88	Mustard (S)	3810	3569	241
2-CEES (Cl)	3810	3704	106	2-CEES (S)	3810	3510	300
Chlorobutane	3810	3722	88	DES	3810	3445	365
Cluster and Adsorbate Values							
Agent	Free Stretching Mode (cm^{-1})	Bound Stretching Mode (cm^{-1})	$\Delta\nu$ (cm^{-1})	Agent	Free Stretching Mode (cm^{-1})	Bound Stretching Mode (cm^{-1})	$\Delta\nu$ (cm^{-1})
Mustard (Cl)	3829	3670	159	Mustard (S)	3826	3517	309
2-CEES (Cl)	3826	3657	169	2-CEES (S)	3826	3370	456
Chlorobutane	3826	3649	177	DES	3826	3271	555

The hydroxyl-stretching mode of the surface model shifts upon adsorption of the adsorbate and is dependent upon the hydrogen bond acceptor of the adsorbate. Evaluation of the hydroxyl-stretching mode shifts indicates in a distinct trend, where sulfur hydrogen bond acceptors result in a larger shift than chlorine acceptors. If the hydrogen bond accepting atom of the adsorbate is a sulfur atom, the hydroxyl mode shift is between 250-555 cm^{-1}. However, if chlorine is the acceptor, the hydroxyl mode shift is between 88-177 cm^{-1}. This trend holds true for all adsorbates.

A trend in binding energy, hydrogen bond length, and hydroxyl-stretching frequency shifts has been shown. The resolution of this information involves the discussion of molecular orbital theory, charge transfer, and the acidity of the bound surface hydroxyl group.

3.2. Discussion

This research, in conjunction with Morris Group at Virginia Tech, explores the differences in binding energy and hydroxyl stretching mode shifts experimentally and

computationally. Detailed analysis of these results has given insight into the hydrogen bonding interaction between the adsorbates and amorphous silica surfaces.

3.2.1. Binding Energies

Experimentally, the activation energy of desorption for all mimic adsorbates was determined by TPD experiments conducted in UHV by Josh Abelard as described in Section 1.2.2.2.[27] The activation energy of desorption and IR data for HD was conducted at Edgewood Chemical Biological Center.[28] The experimentally determined activation energies of desorption, E_d, the counterpoise corrected binding energies at MP2/CBS//B97D/6-31G** for the smaller cluster, and the counterpoise corrected binding energy for the small cluster at the B97D/6-31G** and wB97XD/6-31G** levels of theory for the chloroalkane series are compared in Figure 19.

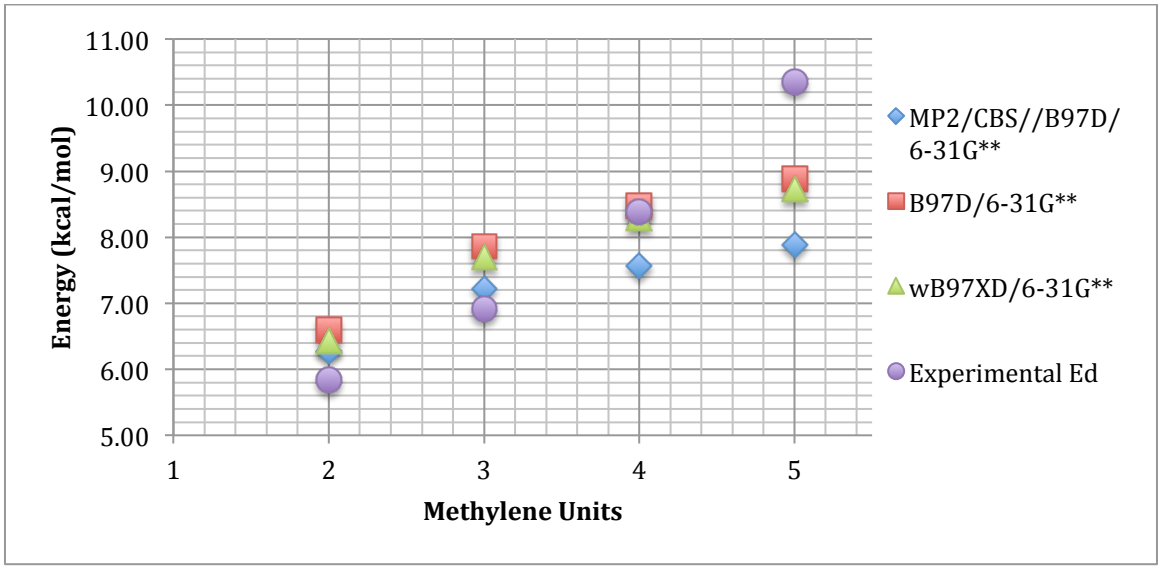

Figure 19. Comparison between the experimental (purple dot) and the small cluster binding energies at B97D/6-31G** (red squares), wB97XD/6-31G**(green triangles), and MP2/CBS//B97D/6-31G**(blue diamonds) levels of theory.

The experimental E_d trend in Figure 19 indicates a positive correlation between number of methylene units and the activation energy of desorption. Each additional methylene unit increases the energy by roughly 1.5 kcal/mol. This is interpreted as each additional methylene group undergoing dispersion interactions with the silica surface. However, the trend for the

computationally determined binding energies is not linear and does not have a continuous positive slope. In the small cluster at B97D/6-31G** and wB97XD/6-31G**, the chloroethane and chlorpropane binding energies agree with the experimental data but deviation occurs at longer chain lengths. This was attributed to the finite structure of the small cluster model. Future work may include the extending of the cluster further to adequately capture the dispersion interactions of the methylene groups of larger chloroalkanes.

The binding energies at the B97D/6-31G** and wB97D/6-31G** levels of theory are compared to those at MP2/CBS//B97D/6-31G**. MP2/CBS is used to benchmark the calculations with a large basis set and a more comprehensive level of theory. All MP2/CBS//B97D/6-31G** binding energies are lower than the B97D and wB97D energies in Figure 19. However, the trend in MP2/CBS//B97D/6-31G** is the same as those in the B97D/6-31G** and wB97XD/6-31G** levels of theory. The similarities in the trends between the three levels of theory suggest that the B97D/6-31G** and wB97XD/6-31G** accurately capture the binding energies and trends. Because the B97D/6-31G** level of theory accurately captures the binding energies and there was no significant difference between B97D/6-31G** and wB97XD/6-31G**, all calculations on sulfur mustard and mimics were carried out using the B97D/6-31G** level of theory.

Table 5. The binding energies at MP2/CBS//B97D/6-31G** and activation energies of desorption in kcal/mol for sulfur mustard and its mimics determined experimentally.[27, 28]

MP2/CBS//6-31G** Binding Energy		Experimental Activation Energy of Desorption	
Adsorbate	Energy (kcal/mol)	Adsorbate	Energy (kcal/mol)
Sulfur Mustard (Cl)	9.29	Sulfur Mustard	9.92 ± 0.05
Sulfur Mustard (S)	8.60		
2-CEES (Cl)	8.19	2-CEES	10.21 ± 0.05
2-CEES (S)	9.40		
Chlorobutane	7.56	Chlorobutane	8.39 ± 0.05
DES	10.56	DES	8.89 ± 0.05

The comparison of theory to experiment continues with HD and its mimics. In Table 5, the binding energies are broken down by the hydrogen bond accepting atom while the experimental E_d are listed by adsorbate. The larger sulfur acceptor binding energy trend continues in the experimental and computational data for the chlorobutane and DES mimics. The discrepancy between energy values for chlorobutane and DES differ by less than 10 and 16%, respectively, which shows good agreement between theory and experiment.

The TPD experiments result in activation energies of desorption that are adsorbate specific and, therefore, might include a mixture of the desorption energy associated with both hydrogen bond donors. Comparing the data, it can be seen for HD and 2-CEES that the experimental activation energies agree well with the binding energies. In the case of 2-CEES, the experimental desorption energy was determined to be just slightly larger than the binding energies associated with each hydrogen bond acceptor in the molecule. The surface in the experiment was previously annealed to 700K, which in accordance with Table 1, implies that it is primarily dominated by isolated hydroxyl groups. This makes bidentate binding in which the adsorbate accepts two hydrogen bonds from the surface, unlikely. If bidentate hydrogen bonding were to occur to the surface, the activation energy of desorption would be roughly two times the binding energy. This is not the case and further supports monodentate binding of 2-CEES to surface hydroxyl groups. This result suggests that, at the gas-surface interface, 2-CEES is adsorbing to the surface through only one of its acceptors. The same argument can be used for HD.

The differences in energy between 2-CEES and HD can be explained by analysis of their chemical structure. 2-CEES is structurally similar to HD, with the exception of an ethane group instead of a chloroethane group. In Figure 20, the Mulliken charge analysis of each molecule is

shown, which highlights the two hydrogen bond accepting groups. In HD, the chlorine atoms have the same partial charge due to their isoelectronic environments. In 2-CEES, however, the chlorine atom has a greater negative charge than in HD. Without the oppos chlorine atom to compete for electron density, the chlorine and sulfur atoms in 2-CEES become more negatively charged. This more negative electronic environment is correlated with slightly larger binding energies, as stronger electrostatic interactions can occur between the adsorbate and the surface.

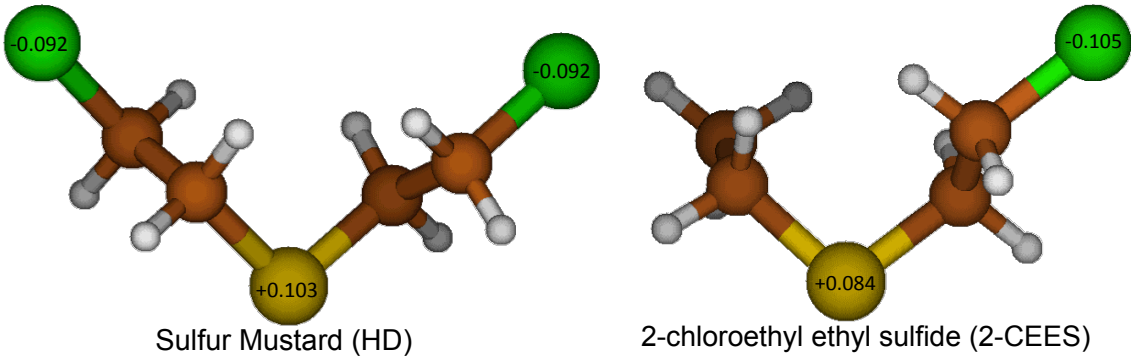

Figure 20. Mulliken charge analysis calculated at the B97D/6-31G** level of theory of the hydrogen bond accepting atoms in sulfur mustard and 2-CEES.

3.2.2. Vibrational Spectra

The trend seen in the frequency shifts associated with the hydroxyl stretching mode gives another clue as to the nature of the hydrogen bonding interaction between the adsorbates and surfaces. Table 4 shows that when sulfur is the hydrogen bond accepting atom, the frequency of the hydroxyl stretching mode red shifts further than when chlorine is the acceptor. This is also seen in experiment. In Figure 21, the experimental IR difference spectrum of 2-CEES, DES, and chlorobutane on amorphous silica are shown and the peaks associated with the hydroxyl stretching mode have been labeled.[27]

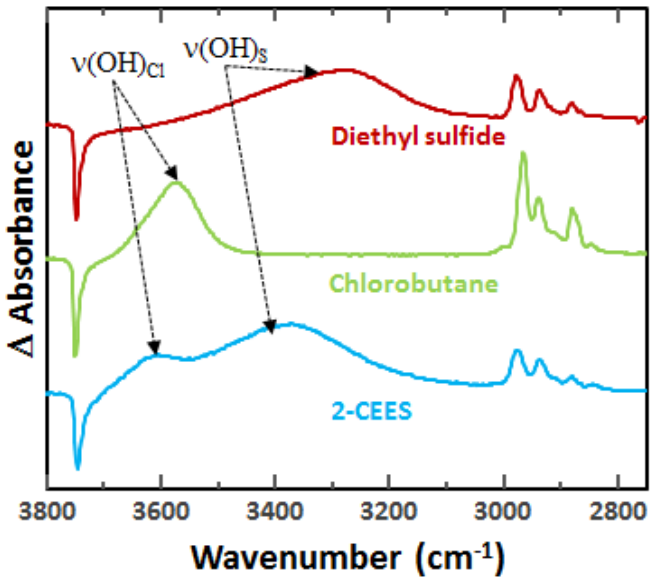

Figure 21. Experimental infrared spectroscopy difference spectrum of diethyl sulfide, chlorobutane, and 2-CEES on amorphous silica in UHV conditions. Reprinted with permission from Abelard, et al. Copyright 2014 American Chemical Society.

In Figure 21, the negative peak at 3750 cm^{-1} is 'free' hydroxyl stretching mode peak, whose intensity has decreased as adsorption has occurred. In the DES spectrum, the peak at 3280 cm^{-1} corresponds to the 'bound' hydroxyl-stretching mode. Similarly, in the chlorobutane spectrum, the red shift is much smaller and results in a peak centered at 3571 cm^{-1}. The 2-CEES spectrum shows two hydroxyl stretching peaks. This indicates that, on the silica surface, 2-CEES molecules adsorb through either the sulfur and chlorine atoms. These modes have shifted to 3598 and 3359 cm^{-1} for chlorine and sulfur acceptors, respectively. Table 6 includes the hydroxyl-stretching mode shifts, with hydrogen bond acceptors indicated in parenthesis, for all adsorbates. In all cases, silica's hydroxyl-stretching mode shifts red upon binding to an adsorbate. Theoretical and experimental shifts are in good agreement and follow the greater sulfur acceptor shift trend. All theoretical shifting values for the adsorbate on the small cluster are greater than those in experiment. To explain these shifting differences, as well as the binding differences, a study of the frontier molecular orbitals was performed.

Table 6. The hydroxyl stretching mode shifts from experimental IR data and calculated spectra for HD[28] and its mimics[27]. All shifts are calculated from the small cluster and adsorbate at B97D/6-31G** with the exception of chlorobutane, where the shift is calculated from the extended cluster at the same level of theory.

Hydroxyl Stretching Mode Shifts						
Agent	Theoretical Small Cluster Calculations			Experimental Infrared Data		
	Free Stretch (cm^{-1})	Bound Stretch (cm^{-1})	$\Delta\nu$ (cm^{-1})	Free Stretch (cm^{-1})	Bound Stretch (cm^{-1})	$\Delta\nu$ (cm^{-1})
Sulfur Mustard (Cl)	3829	3670	159	3750	3615	135
Sulfur Mustard (S)	3826	3517	309	3750	3310	440
2-CEES (Cl)	3826	3657	169	3750	3598	152
2-CEES (S)	3826	3370	456	3750	3359	391
Chlorobutane	3821	3612	209	3750	3571	179
DES	3826	3271	555	3750	3280	470

3.2.2.1. Molecular Orbital Calculations

The molecular orbitals for all adsorbates, cluster, and complexes were calculated at B97D/6-31G**. The frontier orbitals and energies for the adsorbates and both conformers of the cluster model are seen in Figure 22.

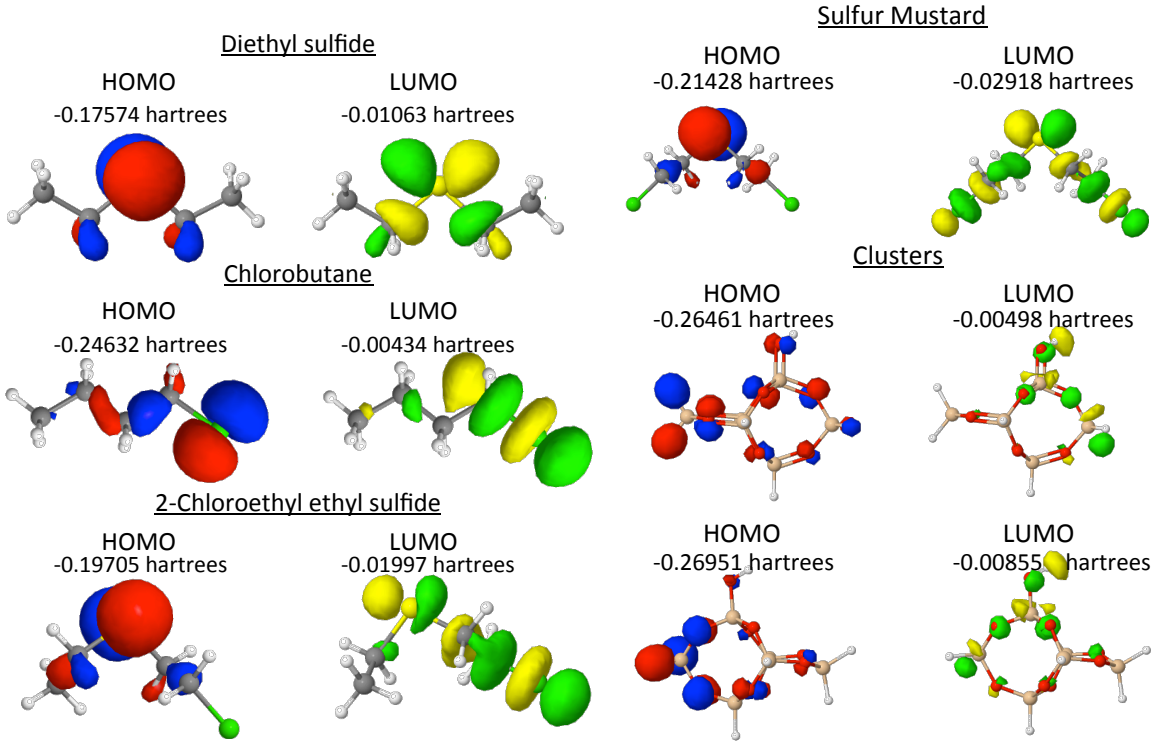

Figure 22. Molecular orbitals and orbital energies for sulfur mustard and its mimics. Energies are calculated at B97D/6-31G** and are in units of hartrees. The HOMOs are in blue and red and LUMOs are in yellow and green.

The frontier orbitals are where the gas-surface interaction between HD and its mimics with silica begins. On the silica surface, the charge-transfer component of adsorption occurs when electron density from the adsorbate is donated into the σ^* anti-bonding orbital of the hydroxyl group. The σ^* anti-bonding orbital of the hydroxyl group is shown in Figure 22 as the LUMO for the cluster, where the orbital density can be seen having a node along the O-H bond. Theorbital on the adsorbate, however, is not as easy to describe.

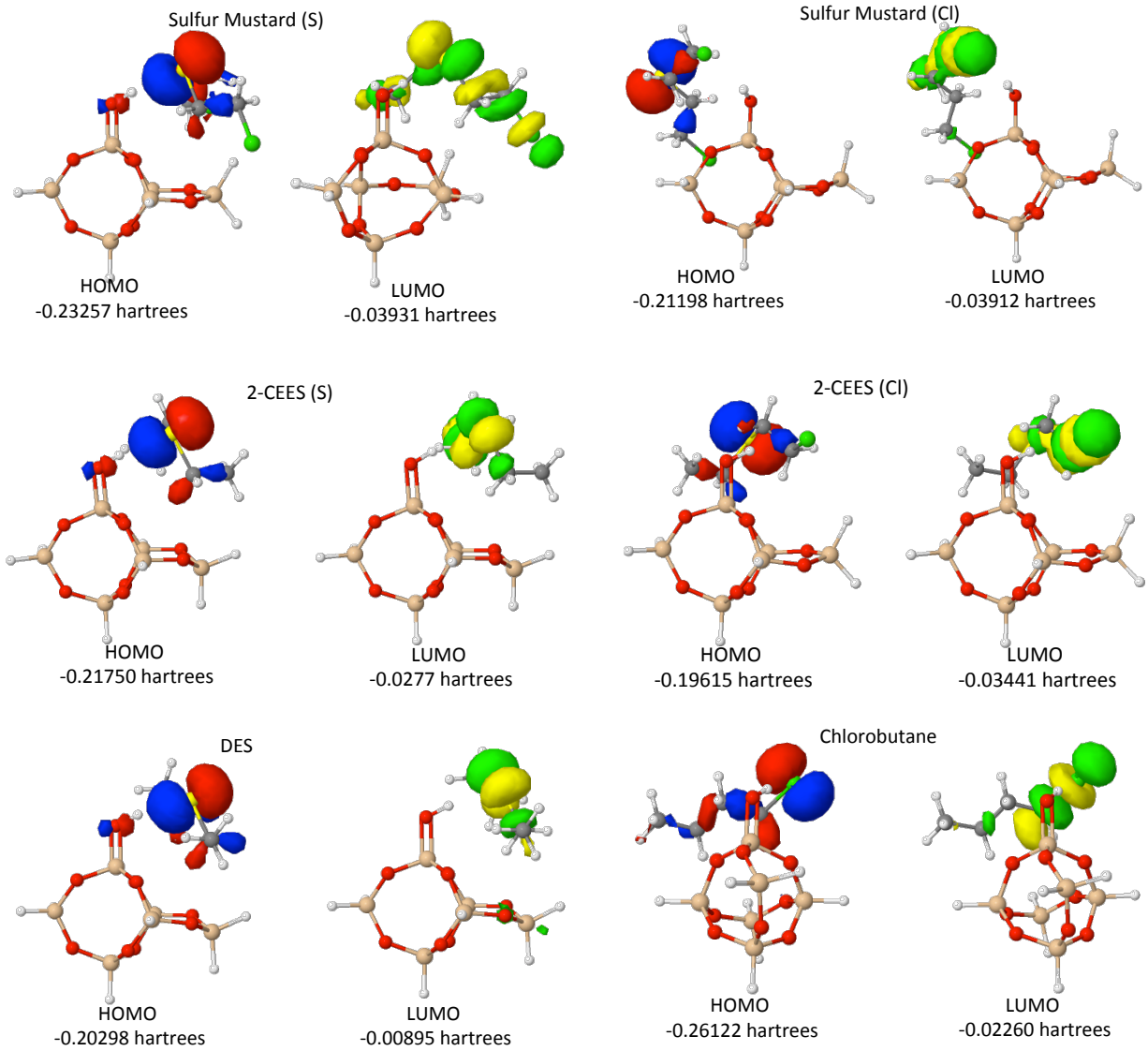

Figure 23. HOMO and LUMO for all complexes of cluster models and adsorbates calculated at B97D/6-31G**. The hydrogen bond acceptor is noted in parenthesis.

When sulfur is the hydrogen bond accepting group, larger hydroxyl stretching mode shifts are seen than in chlorine acceptors. The mode shifts can be explained by the orbital energies of the chlorine and sulfur moieties in the adsorbate. In the case of 2-CEES, the HOMO shows large lobes of orbital density around the sulfur moiety and no orbital density around the chlorine atom. The closest occupied orbital with density around the chlorine atom is one orbital lower in energy than the HOMO. That orbital that has larger chlorine density has an energy of -0.25351 hartrees. The same is true for HD, where the chlorine density rich orbital's energy is -0.26027 hartrees. The strength of the charge-transfer component of the interaction between adsorbate and surface is inversely proportional to the differences in orbital energy. Assuming that the occupied orbital of the adsorbate overlaps with the LUMO of the cluster, large differences in energy between these two orbitals will decrease the charge-transfer portion of the interaction energy. Therefore, when chlorine is the hydrogen bond acceptor, the difference between the LUMO of the cluster and the orbital with electron density in the adsorbate is large and the charge transfer component of the interaction energy decreases. The opposite is true when sulfur is the hydrogen bond donor, as the orbital density around sulfur is higher in energy and closer to the energy of the LUMO. This line of reason can be utilized to explain the hydroxyl-stretching mode shift trend.

The molecular orbitals of the complexes are also useful when explaining the hydroxyl-stretching mode shift trend. In Figure 23, the frontier orbitals and energies for all complexes are shown. In complexes where sulfur is the hydrogen bond accepting group, larger orbital density can be seen between the hydroxyl group and the adsorbate. Specifically, orbital density can be

seen along the hydrogen-bonding axis between the adsorbate and the cluster. This larger orbital overlap leads to stronger charge transfer, as discussed in Section 2.2.3.1. The stronger the interaction between the hydroxyl group and the adsorbate, the weaker hydroxyl bond and the smaller the hydroxyl spring constant becomes. In accordance with Equation 28, a smaller k_i results in a lower $\tilde{\nu}_i$, explains the larger shifts OH stretching shifts seen with sulfur acceptor. This reasoning applies to all adsorbates.

3.2.2.2. Hydroxyl Bond Acidity

The hydrogen bond acidity also plays an important role in the adsorption of HD and its mimics to amorphous silica. The Mulliken charge analysis of the hydroxyl atoms of each adsorbate-cluster complexes are listed below in Table 7. When sulfur is the hydrogen bond acceptor, the partial charge on the hydroxyl hydrogen is higher than when chlorine is the acceptor. This is true in every case. The charge separation between partial charges on the hydrogen and partial charges on the oxygen atoms is also larger in all sulfur acceptors than in chlorine acceptors. The greater the separation between charges, the stronger the electrostatic interaction in the hydroxyl bond will be. This is in agreement with the hydrogen bond acceptor dependent binding energy trend.

Table 7. The partial charges on the hydroxyl hydrogen and oxygen atoms for each adsorbate on the cluster calculated at B97D/6-31G**.

Adsorption on Cluster		
Adsorbate	Partial Charge on Hydroxyl Hydrogen	Partial Charge on Hydroxyl Oxygen
Sulfur Mustard (Cl)	0.339	-0.585
Sulfur Mustard (S)	0.347	-0.583
2-CEES (Cl)	0.337	-0.580
2-CEES (S)	0.343	-0.578
Chlorobutane	0.340	-0.567
DES	0.345	-0.574

3.3. Conclusion and Future Work

In conclusion, the adsorption of sulfur mustard and its mimics to amorphous silica has been studied using computational methods in order to better understand the interaction mechanism. The computational methods have been chosen to include functionals, including B97D, that can account for the long-range dispersion interactions between the adsorbates and the surface and to include basis sets that adequately describe the system. The counterpoise corrected binding energies, vibrational frequencies, and molecular orbitals were analysized for each adsorbate and through each hydrogen bond accepting moiety in each adsorbate. A series of chloroalkanes adsorbed on silica showed that the B97D functional captured an increase in binding energy with additional methylene units due to dispersion interactions. All work on the CWA and its mimics showed that when the sulfur atom was the hydrogen bond accepting atom, the binding energy, the hydroxyl stretching mode shift, and the hydroxyl bond acidity were all greater than when chlorine was the acceptor. These trends were attributed to the differences in orbital energetics and electrostatic interactions as a function of hydrogen bond acceptor.

Future work may include the use of the more extended cluster, which will help capture dispersion interactions of longer molecules and to add linearity to the chloroalkane series. The interaction of aromatic and polyaromatic compounds with amorphous silica may also be investigated computationally. Quantum mechanical and molecular dynamics calculations may be performed on sulfur mustard and its mimics on other surfaces, such as TiO_2, to determine the fate of the CWAs in other environments. Finally, the investigation of toxic industrial compounds adsorbing on atmospheric dust particles may give insight into environmental impact of these gas-surface interactions. The use of computational methods in surface chemistry will continue to be a useful tool to probe these unique interactions.

References

(1) Jovanovic, D. S. *Kolloid-Z. Z. Polym.* **1969**, *235*, 1203.

(2) Erdem, B.; Hunsicker, R. A.; Simmons, G. W.; Sudol, E. D.; Dimonie, V. L.; El-Aasser, M. S. *Langmuir* **2001**, *17*, 2664.

(3) *Colloidal Silica: Fundamentals and Applications*; CRC Press: New York, NY, 2006; Vol. 131.

(4) Wilsmeyer, A. R., Virginia Polytechnic Institute and State University, 2012.

(5) Roy, A.; Srivastava, A. K.; Singh, B.; Shah, D.; Mahato, T. H.; Gutch, P. K.; Halve, A. K. *J. Porous Mater.* **2013**, *20*, 1103.

(6) Corps, U. M. *Change* **2002**.

(7) Wilmsmeyer, A. R.; Gordon, W. O.; Davis, E. D.; Troya, D.; Mantooth, B. A.; Lalain, T. A.; Morris, J. R. *The Journal of Physical Chemistry C* **2013**, *117*, 15685.

(8) Gordon, W. O.; Tissue, B. M.; Morris, J. R. *The Journal of Physical Chemistry C* **2007**, *111*, 3233.

(9) Rusu, C. N.; Yates, J. T. *The Journal of Physical Chemistry B* **2000**, *104*, 12292.

(10) Thompson, T. L.; Panayotov, D. A.; Yates, J. T. *The Journal of Physical Chemistry B* **2004**, *108*, 16825.

(11) Yang, L.; Shroll, R. M.; Zhang, J.; Lourderaj, U.; Hase, W. L. *The Journal of Physical Chemistry A* **2009**, *113*, 13762.

(12) Zhou, X. L.; Sun, Z. J.; White, J. M. *J. Vac. Sci. Technol., A* **1993**, *11*, 2110.

(13) Saxena, A.; Srivastava, A. K.; Singh, B.; Goyal, A. *Journal of Hazardous Materials* **2012**, *211–212*, 226.

(14) Langmuir, I. *J. Chem. Soc.* **1940**, 511.

(15) Czepirski, L.; Balys, M. R.; Komorowska-Czepirska, E. *Internet J. Chem.* **2000**, *3*, No pp. given.

(16) Langmuir, I. *Journal of the American Chemical Society* **1918**, *40*, 1361.

(17) Langmuir, I. *J. Am. Chem. Soc.* **1916**, *38*, 2221.

(18) Barron, A. R. a. H., N. 2011.

(19) Brunauer, S.; Emmett, P. H.; Teller, E. *J. Am. Chem. Soc.* **1938**, *60*, 309.

(20) Bae, Y.-S.; Yazaydin, A. O.; Snurr, R. Q. *Langmuir* **2010**, *26*, 5475.

(21) Kisliuk, P. *Journal of Physics and Chemistry of Solids* **1957**, *3*, 95.

(22) Lipponer, M. A.; Armbrust, N.; Duerr, M.; Hoefer, U. *J. Chem. Phys.* **2012**, *136*, 144703/1.

(23) Tao, J.; Luttrell, T.; Bylsma, J.; Batzill, M. *The Journal of Physical Chemistry C* **2011**, *115*, 3434.

(24) Zhuravlev, L. T. *Langmuir* **1987**, *3*, 316.

(25) Williams, G. H.; Henry Holt and Company: New York, 1890; Vol. 3rd.

(26) Galynska, M.; Persson, P. *Int. J. Quantum Chem.*, Ahead of Print.

(27) Abelard, J. *J. Phys. Chem. C.* **2014**.

(28) Gordon, W. O.; Edgewood Chemical Biological Center: 2014.

(29) Wilmsmeyer, A. R.; Uzarski, J.; Barrie, P. J.; Morris, J. R. *Langmuir* **2012**, *28*, 10962.

(30) Arunan, E.; Desiraju, G. R.; Klein, R. A.; Sadlej, J.; Scheiner, S.; Alkorta, I.; Clary, D. C.; Crabtree, R. H.; Dannenberg, J. J.; Hobza, P.; Kjaergaard, H. G.; Legon, A. C.; Mennucci, B.; Nesbitt, D. J. *Pure Appl. Chem.* **2011**, *83*, 1619.

(31) Bhattacharyya, S.; Bhattacherjee, A.; Shirhatti, P. R.; Wategaonkar, S. *J. Phys. Chem. A* **2013**, *117*, 8238.

(32) Biswal, H. S.; Shirhatti, P. R.; Wategaonkar, S. *J. Phys. Chem. A* **2010**, *114*, 6944.
(33) Biswal, H. S.; Wategaonkar, S. *J. Phys. Chem. A* **2010**, *114*, 5947.
(34) Freindorf, M.; Kraka, E.; Cremer, D. *Int. J. Quantum Chem.* **2012**, *112*, 3174.
(35) Gu, Q.; Trindle, C.; Knee, J. L. *J. Chem. Phys.* **2012**, *137*, 091101/1.
(36) Kumar, S.; Biswas, P.; Kaul, I.; Das, A. *J. Phys. Chem. A* **2011**, *115*, 7461.
(37) Rimola, A.; Costa, D.; Sodupe, M.; Lambert, J.-F.; Ugliengo, P. *Chem. Rev. (Washington, DC, U. S.)* **2013**, *113*, 4216.
(38) Rivera-Rivera, L. A.; McElmurry, B. A.; Scott, K. W.; Lucchese, R. R.; Bevan, J. W. *J. Phys. Chem. A* **2013**, *117*, 8477.
(39) Szostak, R. *Chem. Phys. Lett.* **2011**, *516*, 166.
(40) Weinhold, F.; Klein, R. A. *Mol. Phys.* **2012**, *110*, 565.
(41) Wright, A. M.; Howard, A. A.; Howard, J. C.; Tschumper, G. S.; Hammer, N. I. *J. Phys. Chem. A* **2013**, *117*, 5435.
(42) Zierkiewicz, W.; Michalska, D.; Havlas, Z.; Hobza, P. *ChemPhysChem* **2002**, *3*, 511.
(43) Bermudez, V. M. *The Journal of Physical Chemistry C* **2007**, *111*, 3719.
(44) Taylor, D. E.; Runge, K.; Cory, M. G.; Burns, D. S.; Vasey, J. L.; Hearn, J. D.; Griffith, K.; Henley, M. V. *J. Phys. Chem. C* **2013**, *117*, 2699.
(45) Zhuravlev, L. T. *Colloids and Surfaces A-physicochemical and Engineering Aspects* **2000**, *173*, 1.
(46) Quenneville, J.; Taylor, R. S.; van, D. A. C. T. *J. Phys. Chem. C* **2010**, *114*, 18894.
(47) Lonstad, B. B.-T.; Mino, L.; Giordanino, F.; Beato, P.; Svelle, S.; Lillerud, K. P.; Bordiga, S. *Phys. Chem. Chem. Phys.* **2013**, *15*, 13363.
(48) Liu, H.; Hamers, R. J. *Surface Science* **1998**, *416*, 354.
(49) Lamb, R. N.; Ngamsom, B.; Trimm, D. L.; Gong, B.; Silveston, P. L.; Praserthdam, P. *Appl. Catal., A* **2004**, *268*, 43.
(50) Patterson, M. C.; Nie, X.; Wang, F.; Kurtz, R. L.; Sinnott, S. B.; Asthagiri, A.; Sprunger, P. T. *J. Phys. Chem. C* **2013**, *117*, 18386.
(51) Khan, M. A. K.; Long, Y.-T.; Schatte, G.; Kraatz, H.-B. *Analytical Chemistry* **2007**, *79*, 2877.
(52) Barrie, P. J. *Phys. Chem. Chem. Phys.* **2008**, *10*, 1688.
(53) Darchini-Maragheh, E.; Nemati-Karimooy, H.; Hasanabadi, H.; Balali-Mood, M. *Basic Clin. Pharmacol. Toxicol.* **2012**, *111*, 426.
(54) Hodgson, E.; Rose, R. L. *Drug Metab. Rev.* **2005**, *37*, 1.
(55) Sanderson, H.; Fauser, P.; Thomsen, M.; Soerensen, P. B. *J. Hazard. Mater.* **2009**, *162*, 416.
(56) Timchalk, C.; Hinderliter, P. M.; Poet, T. S.; John Wiley & Sons Ltd.: 2010, p 137.
(57) Wang, Q.; Gu, M.; Feng, J.; Ruan, J. *Fenxi Huaxue* **2006**, *34*, 5.
(58) Hill, B. A., Hilmas, C. J., and Smart, J. K. In *Medical Aspects of Chemical Warfare*.
(59) Chauhan, S.; Chauhan, S.; D'Cruz, R.; Faruqi, S.; Singh, K. K.; Varma, S.; Singh, M.; Karthik, V. *Environmental Toxicology and Pharmacology* **2008**, *26*, 113.
(60) Bermudez, V. M. *The Journal of Physical Chemistry C* **2009**, *113*, 1917.
(61) Bermudez, V. M. *The Journal of Physical Chemistry C* **2010**, *114*, 3063.
(62) Brevett, C. A. S.; Sumpter, K. B.; Pence, J.; Nickol, R. G.; King, B. E.; Giannaras, C. V.; Durst, H. D. *The Journal of Physical Chemistry C* **2009**, *113*, 6622.
(63) Dadvar, S.; Tavanai, H.; Morshed, M.; Ghiaci, M. *Sep. Purif. Technol.* **2013**, *114*, 24.

(64) Ferguson-McPherson, M. K.; Low, E. R.; Esker, A. R.; Morris, J. R. *J. Phys. Chem. B* **2005**, *109*, 18914.
(65) Ferguson-McPherson, M. K.; Low, E. R.; Esker, A. R.; Morris, J. R. *J Phys Chem B* **2005**, *109*, 18914.
(66) Henderson, M. A.; Jin, T.; White, J. M. *J. Phys. Chem.* **1986**, *90*, 4607.
(67) Kanan, S. M.; Tripp, C. P. *Langmuir* **2001**, *17*, 2213.
(68) Kanyi, C. W.; Doetschman, D. C.; Schulte, J. T. *Microporous and Mesoporous Materials* **2009**, *124*, 232.
(69) Panayotov, D.; Kondratyuk, P.; Yates, J. T. *Langmuir* **2004**, *20*, 3674.
(70) Panayotov, D. A.; Morris, J. R. *Langmuir* **2009**, *25*, 3652.
(71) Panayotov, D. A.; Paul, D. K.; Yates, J. T. *The Journal of Physical Chemistry B* **2003**, *107*, 10571.
(72) Siu, E. Y.; Andino, J. M. *NANO* **2008**, *3*, 233.
(73) Štengl, V.; Maříková, M.; Bakardjieva, S.; Šubrt, J.; Opluštil, F.; Olšanská, M. *Journal of Chemical Technology & Biotechnology* **2005**, *80*, 754.
(74) Taranenko, N.; Alarie, J.-P.; Stokes, D. L.; Vo-Dinh, T. *J. Raman Spectrosc.* **1996**, *27*, 379.
(75) Troya, D.; Edwards, A. C.; Morris, J. R. *J. Phys. Chem. C* **2013**, *117*, 14625.
(76) Trubitsyn, D. A.; Vorontsov, A. V. *Computational and Theoretical Chemistry* **2013**, *1020*, 63.
(77) Wagner, G. W.; Bartram, P. W.; Koper, O.; Klabunde, K. J. *The Journal of Physical Chemistry B* **1999**, *103*, 3225.
(78) Wang, L.; Zhu, H.; Cheng, Z.; Ma, M.; Liang, J.; Zhang, X. *Adv. Mater. Res. (Durnten-Zurich, Switz.)* **2013**, *616-618*, 1702.
(79) Parida, S. K.; Dash, S.; Patel, S.; Mishra, B. K. *Advances in Colloid and Interface Science* **2006**, *121*, 77.
(80) Yan, F.; Stokes, D. L.; Wabuyele, M. B.; Griffin, G. D.; Vass, A. A.; Vo-Dinh, T. *Proc. SPIE-Int. Soc. Opt. Eng.* **2004**, *5321*, 302.
(81) Feyereisen, M. W.; Feller, D.; Dixon, D. A. *The Journal of Physical Chemistry* **1996**, *100*, 2993.
(82) Martin, F.; Zipse, H. *J. Comput. Chem.* **2004**, *26*, 97.
(83) Seitzinger, A. T. G., P. S.; White, W. E.; Stuempfle, A. K.; and Birenzvige, A. *Use of Methyl Salicylates As a Trialing Chemical Agent Simulant*, 1990.
(84) Prasad, G. K.; Singh, B.; Saxena, A. *AIChE Journal* **2006**, *52*, 678.
(85) Ishida, H.; Ray, R.; Amnuaysirikul, J.; Ishida, K.; Ray, P. *ISRN Toxicol.* **2012**, 190429.
(86) Praveen, K. J.; Prasad, G. K.; Ramacharyulu, P. V. R. K.; Garg, P.; Ganesan, K. *Mater. Chem. Phys.* **2013**, *142*, 484.
(87) Inscore, F.; Farquharson, S. *Proc. SPIE-Int. Soc. Opt. Eng.* **2006**, *6378*, 63780X/1.
(88) Stout, S. C.; Larsen, S. C.; Grassian, V. H. *Microporous and Mesoporous Materials* **2007**, *100*, 77.
(89) M. J. Frisch, G. W. T., H. B. Schlegel, G. E. Scuseria, M. A. Robb, J. R. Cheeseman, G. Scalmani, V. Barone, B. Mennucci, G. A. Petersson, H. Nakatsuji, M. Caricato, X. Li, H. P. Hratchian, A. F. Izmaylov, J. Bloino, G. Zheng, J. L. Sonnenberg, M. Hada, M. Ehara, K. Toyota, R. Fukuda, J. Hasegawa, M. Ishida, T. Nakajima, Y. Honda, O. Kitao, H. Nakai, T. Vreven, J. A. Montgomery, Jr., J. E. Peralta, F. Ogliaro, M. Bearpark, J. J. Heyd, E. Brothers, K. N. Kudin, V. N. Staroverov, R. Kobayashi, J. Normand, K. Raghavachari, A. Rendell, J. C.

Burant, S. S. Iyengar, J. Tomasi, M. Cossi, N. Rega, J. M. Millam, M. Klene, J. E. Knox, J. B. Cross, V. Bakken, C. Adamo, J. Jaramillo, R. Gomperts, R. E. Stratmann, O. Yazyev, A. J. Austin, R. Cammi, C. Pomelli, J. W. Ochterski, R. L. Martin, K. Morokuma, V. G. Zakrzewski, G. A. Voth, P. Salvador, J. J. Dannenberg, S. Dapprich, A. D. Daniels, Ö. Farkas, J. B. Foresman, J. V. Ortiz, J. Cioslowski, and D. J. Fox In *Wallingford, CT* 2009; Vol. A.1.
(90) Jensen, F. *Introduction to Computational Chemistry*; 2nd ed.; Wiley: England, 2007.
(91) Cramer, C. J. *Essentials of Computational Chemistry: Theories and Models*; J. Wiley & Sons, 2002.
(92) Aharonov, Y.; Anandan, J.; Vaidman, L. *Physical Review A* **1993**, *47*, 4616.
(93) Szabo, A. a. O., N. S. *Modern Quantum Chemistry: Introduction to Advanced Electronic Structure Theory*; Dover Publications: Mineola, New York, 1996.
(94) Chen, J. a. Y., S. In *Van Voorhis group, MIT Chemistry* 2010.
(95) Kohn, W.; Sham, L. J. *Physical Review* **1965**, *140*, A1133.
(96) Cuevas, J. C. 2013; Vol. 2013.
(97) Oliver, G. L.; Perdew, J. P. *Physical Review A* **1979**, *20*, 397.
(98) Gill, P. M. W.; Johnson, B. G.; Pople, J. A.; Frisch, M. J. *Chemical Physics Letters* **1992**, *197*, 499.
(99) Becke, A. D. *Phys. Rev. A: Gen. Phys.* **1988**, *38*, 3098.
(100) Stephens, P. J.; Devlin, F. J.; Chabalowski, C. F.; Frisch, M. J. *J. Phys. Chem.* **1994**, *98*, 11623.
(101) Lee, C.; Yang, W.; Parr, R. G. *Physical Review B* **1988**, *37*, 785.
(102) Grimme, S. *Journal of Computational Chemistry* **2006**, *27*, 1787.
(103) Kolandaivel, P.; Uma Maheswari, D.; Senthilkumar, L. *Computational and Theoretical Chemistry* **2013**, *1004*, 56.
(104) Chai, J.-D.; Head-Gordon, M. *Phys. Chem. Chem. Phys.* **2008**, *10*, 6615.
(105) Dunning, T. H. *The Journal of Chemical Physics* **1989**, *90*, 1007.
(106) Peterson, K. A. In *Advanced Topics in Physical Chemistry* Washington State University; Vol. 2014.
(107) Scheiner, S. *Computational and Theoretical Chemistry* **2012**, *998*, 9.
(108) Civalleri, B. In *Crystal Tutorial Project* 2013; Vol. 2014.
(109) In *Gaussian 09 User's Manual* 2013; Vol. 2014.
(110) Schlegel, H. B. *Theor. Chim. Acta* **1984**, *66*, 333.
(111) Besley, N. A. *Philos. Trans. R. Soc., A* **2007**, *365*, 2799.
(112) Ochterski, J. W. In *help@gaussian.com* 1999; Vol. 2014.
(113) Boys, S. F.; Bernardi, F. *Mol. Phys.* **1970**, *19*, 553.
(114) Zipse, H. In *Computational Chemistry I* 2005.
(115) Sherrill, C. D. Georgia Institute of Technology, 2010.
(116) Novoa, J. J.; Planas, M.; Rovira, M. C. *Chemical Physics Letters* **1996**, *251*, 33.
(117) Davidson, E. R. *The Journal of Chemical Physics* **1967**, *46*, 3320.
(118) Mulliken, R. S. *The Journal of Chemical Physics* **1955**, *23*, 1833.
(119) Esselman In *Molecular Modeling* 2014.
(120) Krapp, A.; Bickelhaupt, F. M.; Frenking, G. *Chemistry – A European Journal* **2006**, *12*, 9196.
(121) Albright, T. A.; Burdett, J. K.; Whangbo, M.-H. *Orbital Interactions in Chemistry, Second Edition*; Wiley, 2013.